

Lucas Timotheo Sanches

# A TITLE GOES HERE

Thesis presented to the Post-Graduation  
program in Physics of Federal University of  
ABC as a requirement for obtaining the title of  
Doctor in Physics.

Advisor: Prof. Dr. Maurício Richartz

Santo André - SP

2022

TIMOTHEO SANCHES, Lucas

TÍTULO:SUBTÍTULO / Lucas Timotheo Sanches - Santo André, Universidade Federal do ABC, 2021.

XX fls. XX cm

Orientador: Maurício Richartz

Tese (doutorado) - Universidade Federal do ABC, Programa de Pós-Graduação em Física, 2021

1. Palavra-chave. 2. Palavra-chave. 3. Palavra-chave. I.

TIMOTHEO SANCHES, Lucas. II. Programa de Pós-Graduação em Física, 2021. III. Título: subtítulo

---

AGRADECIMENTOS, DEDICATÓRIA, ETC...

---



---

## **Abstract**

ABSTRACT HERE.

**Keywords:** Keyword1, keyword2, ...



---

## **Resumo**

RESUMO AQUI.

**Palavras chave:** palavra1, palavra2, ...



# Contents

<b>1</b>	<b>Introduction</b>	<b>11</b>
<b>2</b>	<b>Energy Extraction From Black Hole Binaries</b>	<b>15</b>
2.1	Chapter Introduction . . . . .	15
2.2	A brief review of the Penrose process . . . . .	18
2.2.1	The Kerr spacetime . . . . .	19
2.2.2	The Reissner-Nördstrom spacetime . . . . .	19
2.3	Majumdar-Papapetrou Spacetime . . . . .	19
2.3.1	Spacetime metric . . . . .	19
2.3.2	Motion of charged particles . . . . .	20
2.3.3	Generalized ergosphere . . . . .	22
2.3.4	Negative energy orbits and the Penrose process . . . . .	27
2.3.4.1	Orbits in the $\rho$ - $z$ plane . . . . .	29
2.3.4.2	Orbits in the $z = 0$ plane . . . . .	30
2.3.5	Examples of Penrose processes . . . . .	32
2.3.6	Efficiency of energy extraction . . . . .	35
2.4	CMMR Spacetime . . . . .	37
2.5	CMMR spacetime . . . . .	37
2.5.1	Spacetime metric . . . . .	37
2.5.2	Ergospheres . . . . .	39
2.5.3	Geodesic motion in the $z = 0$ plane . . . . .	44
2.5.4	Negative energy orbits . . . . .	49
2.5.5	Efficiency of energy extraction . . . . .	50
2.6	Geodesic motion in arbitrary space-times . . . . .	52
2.6.1	ADM Decomposition of the geodesic equation . . . . .	52

2.6.2	Observed quantities . . . . .	53
2.6.3	Proposal for investigating the Penrose process in numeric space-times . . . . .	53
2.7	Arbitrary Spacetimes . . . . .	53
<b>3</b>	<b>Numerical Scalar Wave Scattering in GW150914</b>	<b>55</b>
<b>4</b>	<b>Conclusions and perspectives</b>	<b>57</b>

# Chapter 1

## Introduction

One of the most well known predictions of the Theory of General Relativity (GR) is the existence of spacetime oscillations that propagate throughout the universe, the so called, gravitational waves. The first (indirect) evidence of the existence of such waves occurred when Hulse and Taylor observed, in 1975, the binary system PSR B1913+16 [1]. Observational data proved to be compatible with theoretical analysis for neutron star binaries that emit gravitational waves. On the other hand, direct observations, despite being attempted since the 1960's, only became a reality recently in the year 2015, with measurements from the Advanced Laser Interferometer Gravitational-wave Observatory (Advanced LIGO) [2, 3] giving birth to a new era in astronomy and cosmology. These two observations have a common factor: they involve *binary systems*, that is, two astronomical objects that are close enough for their mutual gravitational attraction to cause them to orbit around a common center of mass as they get closer and closer until a catastrophic collision event occurs, releasing huge amounts of energy and angular momentum in the form of gravitational radiation.

So far, no analytic description of a binary system in GR is known. This is due to the extreme complexity of Einstein's equations (a system of 10 coupled non-linear partial differential equations) whose exact solution is known only for very specific systems with a high degree of symmetry. Even if such an exact solution were to be found, it would likely be too large, complicated and impractical to use. Given that in a collision event the nonlinear character of the equations becomes important the problem must be treated numerically, with

## CHAPTER 1. INTRODUCTION

---

the techniques of the field of Numerical Relativity (NR).

The main goal of our work is to investigate how classical and semi-classical effects in GR that are well known to spacetimes containing a single astrophysical object (a star or a black hole), namely the *quasinormal ringdown*, the *Penrose process* and *Hawking radiation* extend to binary systems. To that end, we will work on two fronts: The first is a *semi-analytic* approach in which we will study exact (and analytic) solutions of Einstein's equations that approximate binary black hole systems in static equilibrium. Such solutions allow us to employ numerical and semi-analytic techniques that are well known to our research group. The second is a *numeric* approach in which we (with the help of international collaborators) will use numeric approximations of binary systems that are no longer in static equilibrium for our investigations.

In astrophysical contexts any excess of electric charge in a black hole tends to be quickly neutralized [4]. For this reason, along with the existence and unicity theorems [5, 6], the most accepted description for an astrophysical black hole is given by the Kerr metric. Despite this fact, Einstein's equations when coupled to Maxwell's equations (a system known as the Einstein-Maxwell equations) admits solutions that represent black holes that are charged electrically and/or magnetically. The non-null electric charge allows for the existence of exact many body solutions to the Einstein-Maxwell system. On the semi-analytic front we will make use of such charged spacetime that was obtained independently by S. D. Majumdar [7] and A. Papapetrou [8], also known as the Majumdar-Papapetrou (MP) solution. This solution represents a binary system composed of two extremely charged Reissner-Nördstrom black holes [9]. Despite containing two charged static black holes, the MP solution can be considered a good approximation for a frontal collision of two non-charged black holes if their approximation velocities are much smaller than the speed of light [10].

It's natural to ask if the MP solution can be generalized to represent systems of multiple charged Kerr-Newman black holes, which would add another degree of "realism" to the analytic treatment. It turns out that such generalization exists and were discovered by W. Israel, G. A. Wilson [11] and A. Perjés [12] and became known as the Israel-Wilson-Perjés (IWP) class. Unfortunately, these solutions cannot represent black holes – they instead must always

---

be naked Kerr-Newman singularities. In order to remain more astrophysically relevant, we will employ another class of solutions that is able to describe static Kerr binaries (and not only naked singularities) that was found very recently by Cabrera-Munguia, Manko and Ruiz (CMMR) [13, 14, 15]. In this solution, the Kerr binaries are kept static thanks to a massless “strut” that is represented by a conical singularity that keeps the black holes from colliding. Despite the “nonphysical” strut, such solution was used to compute the shadow of a binary black hole system and showed a good agreement with the shadow computed using a fully numerical binary system, as was shown by Cunha *et. al.* in [16]. The same group showed in [17] that the massless strut does not influence the motion of photons composing the shadow.



# Chapter 2

## Energy Extraction From Black Hole Binaries

### 2.1 Chapter Introduction

In this chapter, we will explore energy extraction from black hole binaries via the Penrose mechanism (also known as the Penrose Process, which we shall abbreviate respectively as PM and PP) in black hole binaries.

The first incarnation of the PM arose as a consequence of the Kerr metric. The Kerr metric is the best known mathematical description of rotating black holes given by the theory of General Relativity [18, 19, 20, 21]. Unlike static black holes, a Kerr black hole is characterized by the existence of a very peculiar region around its event horizon, known as the *ergosphere* or *ergoregion*. Particles that reach the ergosphere can still avoid the event horizon and, hence, are not doomed to end at the spacetime singularity. Nevertheless, any observer lying inside the ergosphere is unavoidably dragged along by the rotational motion of the black hole.

Particles inside the ergosphere may have negative energies (according to a static observer at infinity). Relying on this property, Penrose and Floyd devised a mechanism that allows one to extract energy from a rotating black hole [22]. The idea consists in sending a particle from infinity towards the black hole and assumes that, once inside the ergosphere, it decays into two other particles. If

one of the fragments is counter-rotating with the black hole and has negative energy (which implies that the split happens inside the ergosphere), it will be captured by the black hole, meaning that the other fragment will escape to infinity. Due to the conservation of the four-momentum, the escaping fragment will have more energy and more angular momentum than the incident particle. Rotational energy and angular momentum are, thus, effectively extracted from the black hole.

Our main motivating factor for this investigation was that despite being a well-known process, the PP had not been studied in the context of black hole binaries. We have also found that many recent research endeavors attempt to establish a relation of the PP with observable astrophysical phenomena. The collisional version of the process, for instance, considers multiple particles that collide and scatter in the ergoregion, allowing arbitrarily high center-of-mass energies. This process can potentially act as a mechanism to eliminate dark matter particles near a supermassive black hole [23]. The magnetic Penrose process [24, 25], on the other hand, considers charged particles and black holes surrounded by magnetic fields (originated, for instance, by plasma accretion disks around the black hole). The electromagnetic interaction allows for highly efficient energy extraction schemes, such as the one introduced in Ref. [26] to model the emission of ultra-high energy cosmic rays from supermassive black holes. Furthermore, recent numerical simulations of plasma and jets around Kerr black holes indicate the important role that negative energy particles and the Penrose process play on the total energy flux coming from the black hole's jets [27].

A few comments on the models chosen for representing the binary systems are in order. Firstly, the nomenclature that we use to refer to a BBH is as follows:

**Definition 2.1.1** (Static/Dynamic BBH model). *A static BBH model represents two black holes that **do not** fall towards each other or move in any other way, thus remaining within a fixed location as time passes. This is in contrast to a dynamic BBH model, in which the constituent BHs either collide or move.*

**Definition 2.1.2** (Exact/Approximate BBH model). *An exact BBH model is one that is an exact vacuum solution of Einstein's field equations. An approximate BBH*

*model is one that is not an exact vacuum solution of said equations, and the deviation from vacuum is not considered to be an exotic type of matter but a measure of its “non-exactness”.*

**Definition 2.1.3** (Analytic/Numeric BBH model). *An **analytic** BBH model is one whose entire spacetime metric is analytically known at all points and times. In contrast, a **numeric** BBH model is obtained only at a certain coordinate time hypersurface (typically  $t = 0$ ) by solving the ADM constraint equations for a vacuum configuration numerically. Note that even though such numerical solutions contain errors, and thus do not strictly solve the vacuum field equations (giving rise to constraint violations), we do not consider these to be approximate, since it’s possible (at least in theory but not in practice due to physical limitation of machines and computational resources) to obtain these solutions with arbitrarily small constraint violations given that they are convergent.*

Secondly, any study that aims to model astrophysical binary systems must acknowledge the fact that there is no known exact and analytical solution of Einstein’s equations describing such a system. Even if exact numerical or approximate analytical solutions are employed, the resulting spacetime metrics are non-stationary and thus limiting the applicability of the standard concept of an ergosphere. Recognizing these difficulties, we have utilized BBH models that are static, exact and analytic.

Our first task was to investigate the possibility of energy extraction from the Majumdar-Papapetrou (MP) metric [7, 8], which is an exact solution of Einstein’s equations that describes a static binary of extremely charged black holes. Despite its mathematical simplicity, the MP solution has recently been used as a surrogate model for black hole binaries in order to understand how single black hole phenomena transpose to a binary system. For instance, Ref. [28] has employed the MP metric to understand the connection between quasinormal modes and light rings in the context of black hole binaries. Refs. [29, 30], on the other hand, have computed the shadows cast by an MP binary to better understand chaotic scattering in a binary black hole system. The resulting shadow shares many similarities and qualitative features with the shadows computed in Ref. [31] using a numerically simulated binary black hole back-

ground. Ref. [10] has also applied the MP metric to analyze particle scattering around a black hole binary and asserted its effectiveness in approximating a head on collision in the limit of large separations and small approach speeds. We followed an analog approach in order to gain physical intuition and qualitative insights about energy extraction from black hole binaries by the Penrose mechanism. In particular, we extended the concept of a particle dependent *generalized ergosphere* [32], which enables the extraction of electromagnetic energy from Reissner-Nördstrom (RN) black holes (as shown in Sec. 2.2.2), to the MP solution and study how the energy extraction efficiency is affected by the presence of a companion black hole.

Taking into account the fact that, in astrophysical contexts, any excess of electric charge in a black hole tends to be quickly neutralized [4], we also considered rotating systems in our work. More specifically, in order to illustrate how the main results for the MP spacetime can be extrapolated to a binary system composed of Kerr black holes, we employ a static exact and analytic solution of Einstein's field equations, discovered independently by Cabrera-Munguia, Manko and Ruiz (hereby referred to as the CMMR metric) [33, 34, 35]. The CMMR metric describes two generic Kerr black holes that do not coalesce thanks to the presence of a "strut" that holds them apart at a fixed distance. In particular, we sketched the ergosphere of the CMMR spacetime for a selected set of parameters and gave an example of a Penrose process around a binary of rotating black holes.

The combined results presented in Sections 2.3 and 2.4 have been compiled in a paper and were published Ref. [36]. As an extension to this work, we have begun the development of a framework that should allow one to observe the PP for an arbitrary spacetime and shall present these results in Sec. 2.7

## 2.2 A brief review of the Penrose process

In this section, we shall briefly review energy extraction of rotating and charged black holes via the Penrose Process to familiarize the reader with the underlying physical concepts, methods and techniques involved in the mechanism. This is important since these tools will be necessary later on while we present novel

results.

### 2.2.1 The Kerr spacetime

Our review will follow closely Ref. [37]

### 2.2.2 The Reissner-Nördstrom spacetime

Review RN

## 2.3 Majumdar-Papapetrou Spacetime

In this section we will show that energy can be extracted from the MP spacetime using the Penrose process. Since the MP spacetime consists of a binary of Reissner-Nördstrom constituents, we will use an electrically charged particle to extract electromagnetic energy from the system.

### 2.3.1 Spacetime metric

For two black holes of masses  $M_1$  and  $M_2$  and electric charges  $Q_1 = M_1$  and  $Q_2 = M_2$ , in equilibrium and separated by a distance  $2a$  along the  $z$ -axis, the MP line element, in Weyl's cylindrical coordinates, is given by [38]

$$ds^2 = -U(\rho, z)^{-2}dt^2 + U(\rho, z)^2[d\rho^2 + \rho^2d\phi^2 + dz^2], \quad (2.1)$$

where

$$U(\rho, z) = 1 + \frac{M_1}{\sqrt{\rho^2 + (z + a)^2}} + \frac{M_2}{\sqrt{\rho^2 + (z - a)^2}}. \quad (2.2)$$

The components of the electromagnetic potential  $A_\mu$  associated with the MP solution are

$$A_\mu = \left(1 - \frac{1}{U}\right)\delta_{\mu t}, \quad (2.3)$$

where  $\delta_{\mu\nu}$  is the Kronecker delta.

We remark that Weyl's coordinates describe only the exterior of the black holes, in such a way that their event horizons and their interiors are collapsed into the points  $\rho = 0, z = \pm a$ . In particular, due to its staticity, the MP spacetime does not possess an ergosphere (in the usual sense of a spacetime region outside the event horizon where it is impossible for freely-falling particles to "stand still" – i.e remain static – while still being able to escape to infinity). In view of that, and motivated by the possibility of Penrose processes for single charged black holes, instead of analysing geodesic motion we will start by studying the trajectories of charged particles in the MP spacetime.

### 2.3.2 Motion of charged particles

The motion of a massive charged test particle (with charge-to-mass ratio  $\mu$ ) in any given spacetime with metric  $g_{\mu\nu}$  and electromagnetic potential  $A_\mu$  is governed by the Lagrangian

$$\mathcal{L} = \frac{1}{2}g_{\mu\nu}\dot{x}^\mu\dot{x}^\nu - \mu A_\alpha\dot{x}^\alpha, \quad (2.4)$$

where  $x^\mu = x^\mu(\lambda) = (t(\lambda), \rho(\lambda), \phi(\lambda), z(\lambda))$  denotes the particle's position (parametrized by its proper time  $\lambda$ ) and dots represent derivatives with respect to  $\lambda$ . Taking into account the explicit form of the MP metric and of the MP electromagnetic potential, the Lagrangian (2.4) can be recast as [39]

$$\mathcal{L} = \frac{1}{2}\left[-\frac{\dot{t}^2}{U^2} + U^2(\dot{\rho}^2 + \rho^2\dot{\phi}^2 + \dot{z}^2)\right] - \mu\left(1 - \frac{1}{U}\right)\dot{t}. \quad (2.5)$$

Since the expression above does not depend explicitly on the coordinates  $t$  and  $\phi$ , two constants of motion can be identified, namely the energy divided by the mass of the particle (as measured by a freely-falling observer at infinity),

$$E \equiv -\frac{\partial\mathcal{L}}{\partial\dot{t}} = \frac{\dot{t}}{U^2} + \mu\left(1 - \frac{1}{U}\right), \quad (2.6)$$

and the angular momentum about the  $z$  axis divided by the mass of the particle (as measured by a freely-falling observer at infinity),

$$L \equiv \frac{\partial \mathcal{L}}{\partial \dot{\phi}} = U^2 \rho^2 \dot{\phi}. \quad (2.7)$$

Plugging these constants of motion into the 4-velocity normalization condition,  $\dot{x}^\mu \dot{x}_\mu = -1$ , and solving for the energy  $E$ , yields

$$E = \mu \left( 1 - \frac{1}{U} \right) + \sqrt{\frac{L^2}{\rho^2 U^4} + \frac{1}{U^2} + \dot{\rho}^2 + \dot{z}^2}, \quad (2.8)$$

where the negative root has been neglected due to the fact that  $E$  must be positive at infinity when  $\mu = 0$  (for a detailed discussion about positive and negative root states for  $E$  see Ref. [32]). We note that Eq. (2.8) reduces to the expression found in Ref. [40] for a Reissner-Norström black hole if the mass of one of the black holes is taken to be zero and an appropriate coordinate system, centered around the other black hole, is used.

Finally, the equations of motion are obtained directly from the Euler-Lagrange equations. After using Eq. (2.6) and Eq. (2.7) to eliminate  $\dot{t}$  and  $\dot{\phi}$  from the resulting expressions, one is left with

$$\ddot{\rho} - \frac{L^2(U + \rho \partial_\rho U)}{\rho^3 U^5} + \frac{2\dot{\rho}\dot{z}\partial_z U - (E^2 + \dot{z}^2 - \dot{\rho}^2)\partial_\rho U}{U} - \frac{\mu}{U} \left( \mu - 2E + \frac{E - \mu}{U} \right) \partial_\rho U = 0, \quad (2.9)$$

and

$$\ddot{z} - \frac{L^2 \partial_z U}{\rho^2 U^5} + \frac{2\dot{\rho}\dot{z}\partial_\rho U - (E^2 - \dot{z}^2 + \dot{\rho}^2)\partial_z U}{U} - \frac{\mu}{U} \left( \mu - 2E + \frac{E - \mu}{U} \right) \partial_z U = 0, \quad (2.10)$$

which reduce to the equations of motion found in Ref. [28] for neutral particles. Together with Eqs. (2.6) and (2.7), the two equations above fully determine the trajectory of a massive charged particle in the MP spacetime once appropriate initial conditions have been specified.

### 2.3.3 Generalized ergosphere

The possibility of extracting energy from a black hole through the Penrose mechanism is intimately linked to the existence of negative-energy trajectories (as measured by observers far away from the black hole). As explained before, in the MP spacetime (and in other static spacetimes like Reissner-Nordstrom) there are no ergospheres in the usual sense, meaning that geodesic motion is always associated with positive energy trajectories. Any charged particle moving through the MP spacetime, however, will be affected by Lorentz forces from its electromagnetic interaction with the black holes and, consequently, will satisfy the equations of motion derived in the previous section. Even though there are no ergospheres in MP, since the trajectories associated with Eqs. (2.6), (2.7), (2.9) and (2.10) are not geodesics, negative values for the constant of motion  $E$  are not forbidden *a priori*. If negative energy trajectories exist in the MP spacetime, then one can define generalized ergospheres as the regions of spacetime where they are allowed to exist. The concept of generalized ergospheres is not new, however, and was first introduced by Denardo and Ruffini for the Reissner - Nordström solution in Ref. [40], where they have additionally shown that the Penrose process is viable in this spacetime by presenting concrete examples. That being said, defining a generalized ergosphere for the MP spacetime is a natural step forward from D. and R. since it consists of two extremely charged RN black holes.

From Eq. (2.8) it is evident that, for fixed  $\mu$ , the energy is completely determined by the angular momentum  $L$ , and the values of  $\rho$ ,  $z$ ,  $\dot{\rho}$  and  $\dot{z}$  at any given instant of time. Therefore, at a fixed position in space, the minimum possible energy is associated with particles at rest. Letting  $\dot{\rho} = \dot{z} = 0$  and  $L = 0$  (i.e.  $\dot{\phi} = 0$ ), we conclude that the minimum energy  $E_{\min}$  for a particle, as a function of its position, is

$$E_{\min} = \mu \left( 1 - \frac{1}{U} \right) + \frac{1}{U}. \quad (2.11)$$

By requiring the minimum energy to be negative, we find that  $\mu$  must necessarily be negative (which means that the particle's charge is opposite to the charge of the black holes) and that the particle (at rest) must be inside the spa-

tial region determined by

$$\frac{M_1}{\sqrt{\rho^2 + (z+a)^2}} + \frac{M_2}{\sqrt{\rho^2 + (z-a)^2}} > -\frac{1}{\mu}. \quad (2.12)$$

Since  $\mu$  is a dimensionless quantity, it makes sense to recast the left side of (2.12) as a dimensionless quantity as well so that we are comparing two pure numbers. To do so, one must simply divide both numerators and denominators of the left side of the inequality by, say,  $M_1$  and define  $\bar{\rho} \equiv \rho/M_1$ ,  $\bar{z} \equiv z/M_1$ ,  $M \equiv M_1/M_2$ ,  $\alpha = a/M_1$  to obtain

$$\frac{1}{\sqrt{\bar{\rho}^2 + (\bar{z} + \alpha)^2}} + \frac{M^{-1}}{\sqrt{\bar{\rho}^2 + (\bar{z} - \alpha)^2}} > -\frac{1}{\mu}. \quad (2.13)$$

This last inequality determines the generalized ergosphere of the MP spacetime as a region depending only on three dimensionless parameters:  $M$ ,  $\alpha$  and  $\mu$ . Particles with charge-to-mass ratio  $\mu$  inside the region determined by (2.13) can have negative energies, while particle outside will never have negative energies. Note that this notion of ergosphere depends not only on the geometry of the spacetime, but also on properties of the particle.

In order to have a graphical representation of the generalized ergosphere, let us use cartesian-like coordinates, also reescaled by  $M_1$ ,  $(\bar{x}, \bar{y}, \bar{z})$  related to Weyl's coordinates by  $\bar{x} = \bar{\rho} \cos \phi$  and  $\bar{y} = \bar{\rho} \sin \phi$ . In Figs. 2.1a-2.1d, we plot the generalized ergosphere for a MP black hole binary of unitary mass-ratio  $M$ , whose horizons (represented by red dots) have also unitary separation parameter  $\alpha$ . As the value of  $\mu$  increases, one can observe that the generalized ergosphere splits into two disconnected spherical regions with the same (albeit smaller than the original) radius. Thus we see that the bigger the value of  $\mu$ , the closer to the horizon an orbit must be in order to realize energy extraction. Extrapolating this result makes it easy to see that the maximum possible amount of energy can only be extracted if a particle is orbiting exactly *at* the event horizon. We will explore this fact further in another section of this work but this result is in agreement with [32].

In Figs. 2.2a-2.2b, we turn to the influence of the mass-ratio in the generalized

ergosphere's shape while keeping fixed  $\mu = -1$  and  $\alpha = 1$ . The ergosphere starts off with the same shape as in Fig. 2.1a. As the mass-ratio increases, the ergosphere around one of the black holes is enlarged while the other's shrunken until a split-up occurs, and again, one ends up with two disconnected regions but this time of different sizes, the larger of which is centered around the heavier black hole. Again, this is to be expected. Because the MP solution represents extremely charged black holes, as the mas of the objects increase (or decrease) so does their electric charge thus allowing for more energy to be extracted and consequently a larger generalized ergosphere.

Finally, in Figs. 2.3a-2.3b we show the effects on the generalized ergosphere resulting from the increase in the distance parameter  $\alpha$  with  $M = 1$  and  $\mu = -1$  fixed. Initially the ergosphere is shaped as in Fig. 2.1a. Yet again, as the value of  $\alpha$  increases, the ergosphere becomes elongated along the  $z$  direction, assuming a ‘peanut’-like shape until it is split into two disconnected regions. From (2.13), we can verify that the splitting occurs when  $\alpha = -(M^{-1} + 1)\mu$ . If the black holes are moved further apart, the system will eventually behave as two isolated extremal black holes of mass  $M$ , each one surrounded by its own spherical generalized ergosphere.

It's also very important to point out that for small separations the generalized ergosphere of the binary system becomes equal to the one around a single RN black hole of mass  $M_1 + M_2$ . One can easily see that by taking the limit  $a \rightarrow 0$  in (2.12) and going to spherical coordinates, related to Weyl's coordinates through  $\rho = \sin \theta$  and  $z = r \cos \theta$ , which leads to the conclusion that the generalized ergosphere is the spherical region centered around the origin which satisfies  $r < -\mu(M_1 + M_2)$ . This is precisely the same region as the one presented in Eq. (12) of Ref. [40] if one considers an extremal black hole in coordinates such that the event horizon is a point at the origin (which amounts the transformation  $r \rightarrow r + M$ ) with the RN solution's mass parameter  $M$  replaced by the total mass of the binary system,  $M_1 + M_2$ .

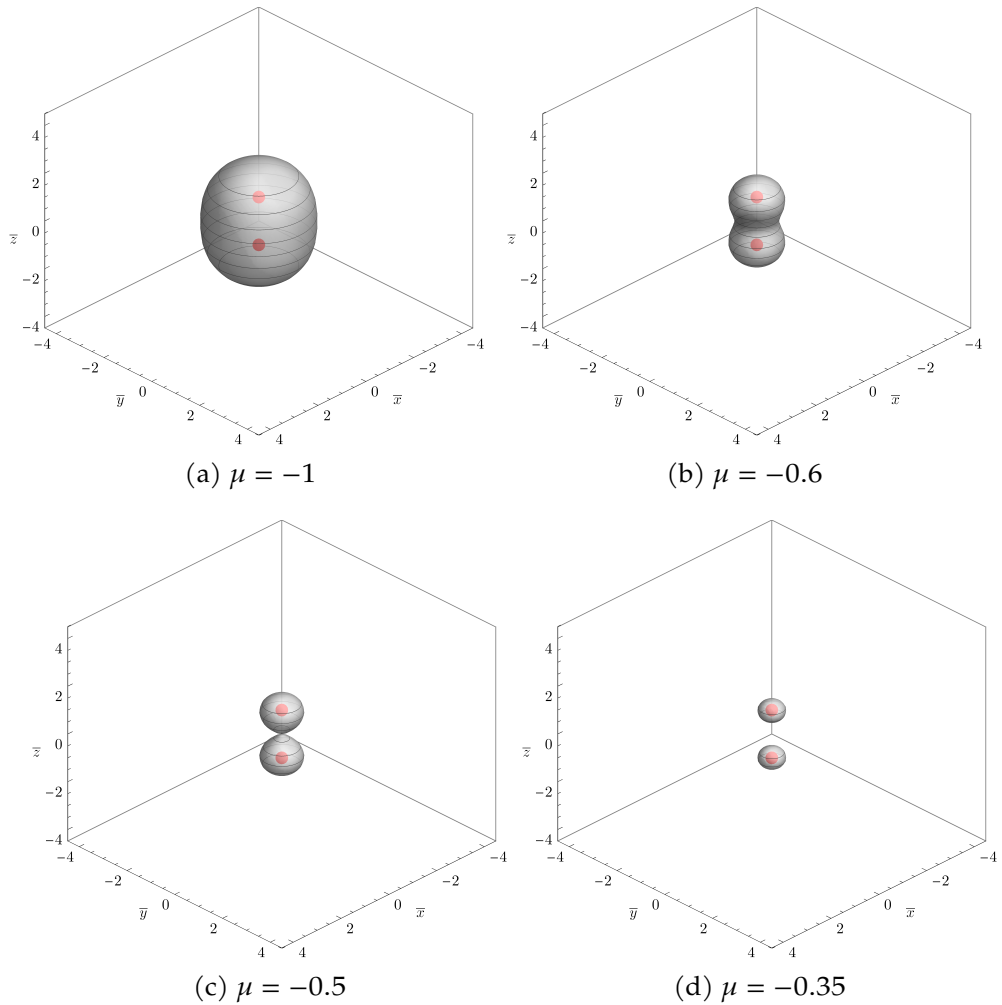


Figure 2.1: Splitting and shrinking of the generalized ergosphere caused by an increase in the charge-to-mass ratio  $\mu$  of a test particle. The separation parameter and mass-ratio are kept fixed at  $\alpha = 1$  and  $M = 1$ , respectively. Note that the splitting produces two symmetric regions that are closer to the horizons.

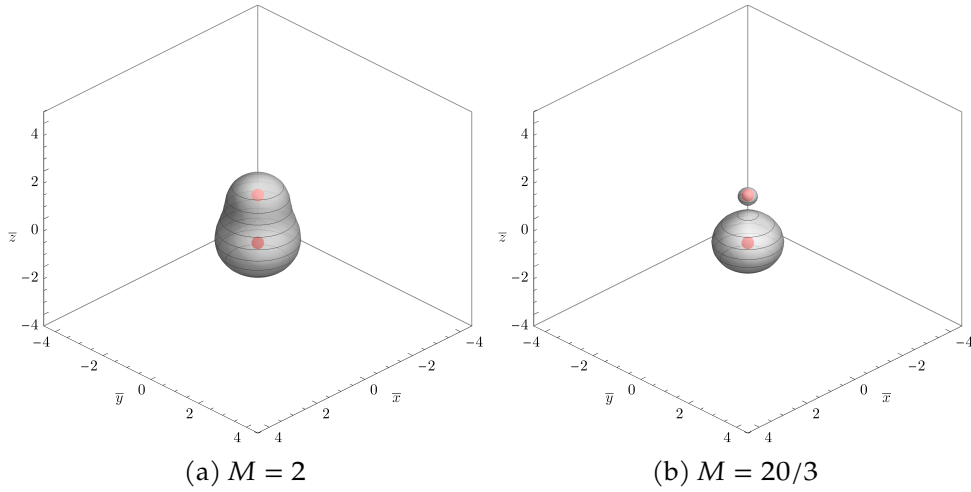


Figure 2.2: Splitting of the generalized ergosphere caused by an increase in the mass ratio  $M$ . The separation parameter and charge-to-mass ratio are kept fixed at  $\alpha = 1$  and  $\mu = -1$ , respectively. The final region is much larger around the heavier black hole.

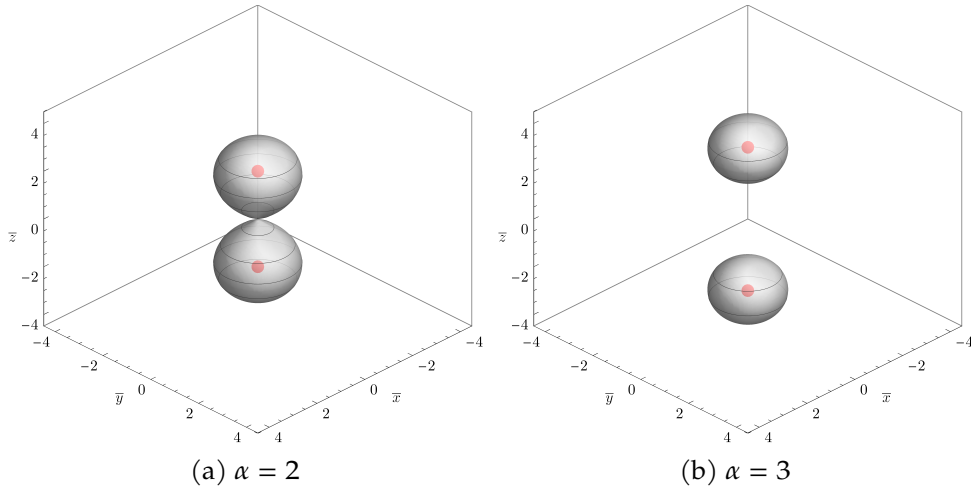


Figure 2.3: Splitting of the generalized ergosphere caused by an increase in the distance parameter  $\alpha$ . The mass ratio and charge-to-mass ratio are kept fixed at  $M = 1$  and  $\mu = -1$ , respectively. The split region is symmetric and it is not closer farther than it previously was to either horizon.

### 2.3.4 Negative energy orbits and the Penrose process

Having understood the notion of generalized ergospheres around binary black holes described by the MP metric, we are now in position to analyze the possibility of energy extraction in such spacetimes. The idea follows Penrose's original proposal [22] and its extension to RN black holes [32, 40]. The mechanism we shall explore consists in sending a negatively charged particle from sufficiently far away towards the binary black hole. Once the particle enters the generalized ergosphere, we need it to break up into two pieces. Depending on how the splitting process is set up, one of the pieces will escape back to infinity with more energy than the incident particle had.

In order to accomplish this one needs three trajectories. The first one, with positive energy  $E^{(0)} > 0$  and labeled  $T^{(0)}$ , must start outside the ergosphere and end inside it, at the point where the other two trajectories, labeled  $T^{(1)}$  and  $T^{(2)}$  start. One of them, let us say  $T^{(1)}$ , must have negative energy, i.e.  $E^{(1)} < 0$ , and, therefore, will remain confined inside the ergosphere. The other one,  $T^{(2)}$ , on the other hand, will have positive energy  $E^{(2)} > E^{(0)}$ , which allows it to escape the ergosphere and reach back infinity.

Suppose that the break-up of the particle occurs at  $(\rho_0, \phi_0, z_0)$ . Let  $m^{(i)}$  and  $P^{(i)}_\mu$  denote, respectively, the mass and the the 4-momentum of the particle on trajectory  $T^{(i)}$ . The conservation of the four-momentum, applied at the break-up point, reads

$$P^{(0)}_\mu = P^{(1)}_\mu + P^{(2)}_\mu. \quad (2.14)$$

Each component of the vector equation above yields a different conservation equation with straightforward physical interpretation. The zero-component, for a start, is just the conservation of total energy, i.e.

$$m^{(0)}E^{(0)} = m^{(1)}E^{(1)} + m^{(2)}E^{(2)}, \quad (2.15)$$

while the angular component is simply the conservation of angular momentum around the  $z$  axis, namely

$$m^{(0)}L^{(0)} = m^{(1)}L^{(1)} + m^{(2)}L^{(2)}. \quad (2.16)$$

The other two components represent the conservation of linear momentum along the radial direction and along the  $z$  axis, respectively

$$m^{(0)}\dot{\rho}^{(0)} = m^{(1)}\dot{\rho}^{(1)} + m^{(2)}\dot{\rho}^{(2)} \quad (2.17)$$

and

$$m^{(0)}\dot{z}^{(0)} = m^{(1)}\dot{z}^{(1)} + m^{(2)}\dot{z}^{(2)}, \quad (2.18)$$

where all the derivatives are to be evaluated at the break-up point  $(\rho_0, \phi_0, z_0)$ .

Because we've assumed that  $E^{(1)} < 0$ , it's easy to see from (2.15) that the particle on trajectory  $T^{(2)}$  will be more energetic than the particle on trajectory  $T^{(0)}$  and thus it has *gained* energy during the split-up process. Obviously this extra energy must come from somewhere. In Penrose's original proposal, the extra energy came from a small loss of angular momentum in the background Kerr black hole. This idea can be readily extended to charged black holes: now instead of angular momentum, the black hole donates part of its electromagnetic energy to an outgoing particle. One might naturally ask how much energy can be extracted using this process. This was not answered by Penrose but by Christodoulou in Ref. [41]. It turns out that the mass of a black hole cannot be smaller than a certain *irreducible mass*, and about 50% of a charged black hole's electromagnetic energy and 29% of a rotating black hole's angular momentum can be extracted through this process. An important variation of the Penrose process is to consider particle collisions, instead of break-ups. This is befittingly known as the collisional Penrose process and it is capable of producing much more energetic ejecta that could be a potential source of gamma rays and high energy cosmic rays (see e.g. [42]), however, in our work we will only focus on the non-collisional version the Penrose process.

The existence of a generalized ergosphere as we've shown, indicates that negative energy orbits can exist and thus electromagnetic energy can be extracted from a MP binary through the Penrose process. However we are not only interested in where these orbits are located but also on some of their features, e.g., whether they fall into one of the black holes or keep orbiting the system in a closed orbit. In the following sections we will describe briefly the characteristics of negative energy orbits constrained to two planes of motion

around the system. This analysis will come into play later when we construct two explicit examples of the penrose process in action. We start by introducing two quantities, the *effective energy*  $E_{\text{eff}}(\rho, z)$  and the *effective potential*  $V_{\text{eff}}(\rho, z)$ , given by

$$E_{\text{eff}}(\rho, z) \equiv E - \mu \left( 1 - \frac{1}{U(\rho, z)} \right) \quad (2.19)$$

and

$$V_{\text{eff}}(\rho, z) \equiv \frac{L^2}{\rho^2 U(\rho, z)^4} + \frac{1}{U(\rho, z)^2}. \quad (2.20)$$

With that, we can recast Eq. (2.8) as

$$\dot{\rho}^2 + \dot{z}^2 = E_{\text{eff}}(\rho, z)^2 - V_{\text{eff}}(\rho, z). \quad (2.21)$$

#### 2.3.4.1 Orbits in the $\rho$ - $z$ plane

One can easily see that by setting  $L$  (and thus  $\dot{\phi}$ ) to zero, the particle's orbit will be constrained to a plane that contains both of the black holes, which we call the  $\rho$ - $z$  plane. Because of the system's cylindrical symmetry one can set  $\phi = 0$  without any loss of generality. To be able to integrate the equations of motion (2.9) and (2.10) one must specify the remaining 4 initial conditions for  $\rho, z$  and their time derivatives. Note however that  $E, \dot{\rho}$  and  $\dot{z}$  are related through (2.21) and thus it suffices to choose  $\rho(0), z(0), \dot{z}(0)$  and  $E$  while using (2.21) to determine  $\dot{\rho}(0)$ .

In order to visualize the orbits we employ once again Cartesian-like coordinates  $(\bar{x}, \bar{y}, \bar{z})$  reescaled by  $M_1, M$  as the system's mass-ratio and  $\alpha$  as its separation parameter. In Figs. 2.4a and 2.4b the event horizons are represented by black dots and the spacetime parameters were fixed at  $M = \alpha = 1$ . Additionally, because our process for finding  $\dot{\rho}(0)$  involves square roots we use solid black lines for orbits resulting from the positive solution and dashed black lines for the negative solution. By extensively testing for many different initial conditions, we found that most orbits end up in either of the two black holes as in Fig. 2.4a. This is not surprising, as particles that follow negative energy orbits

must always be charged oppositely to the black holes and thus they will always be electrically attracted towards the horizons. On the other hand, by choosing parameters very carefully, one is able to find highly unstable but closed orbits as in Fig. 2.4b.

At a first glance, closed negative energy orbits might cause some concern as they never fall into one of the horizons and thus never effectively interact with the black holes to cause them to loose a small amount of electric charge but one must keep in mind that in the MP spacetime such orbits are always unstable and are completely within the generalized ergosphere. Additionally, the existence of closed negative energy orbits is not an exclusive feature of the MP metric. Usually these orbits occur only *inside* event horizons or in naked singularities. Stuchlik has shown in Ref. [43] that there can exist stable circular orbits of negative energy around a Kerr naked singularity and that the Penrose process can effectively take place using said orbits. Patil and collaborators in Ref. [44] have even used this fact to construct a model to explain the origin of ultra high energy particles detected on Earth as a result of the collisional Penrose process in a slightly over spinning Kerr black hole. Similarly, Mukherjee and Nayak in Ref. [45] have used the collisional Penrose process in a Kerr naked singularity with orbits outside the equatorial plane to construct a model for energetic outgoing particle jets. In some situations though, closed negative energy orbits can exist outside of the event horizon as Prasana and Dadhich have shown in Ref. [46] in the spacetime of a Kerr black hole immersed in an external magnetic field that is regular up to the event horizon. More recently Felice and collaborators in Ref. [47] also have shown that magnetized particles in a Kerr black hole can give rise to stable circular orbits of negative energy inside the ergosphere. Therefore, these unstable orbits that we've found are not violating any underlying fundamental principle.

#### 2.3.4.2 Orbits in the $z = 0$ plane

If we set  $z(0) = \dot{z}(0) = 0$  we confine the particle's motion to the plane exactly in between the two black holes and once the background spacetime parameters have been set the trajectory can now be readily determined using only Eq. (2.21) with appropriate values for  $\rho(0)$ ,  $\phi(0)$ ,  $L$ ,  $E$  and  $\mu$ . Thanks to the constrained

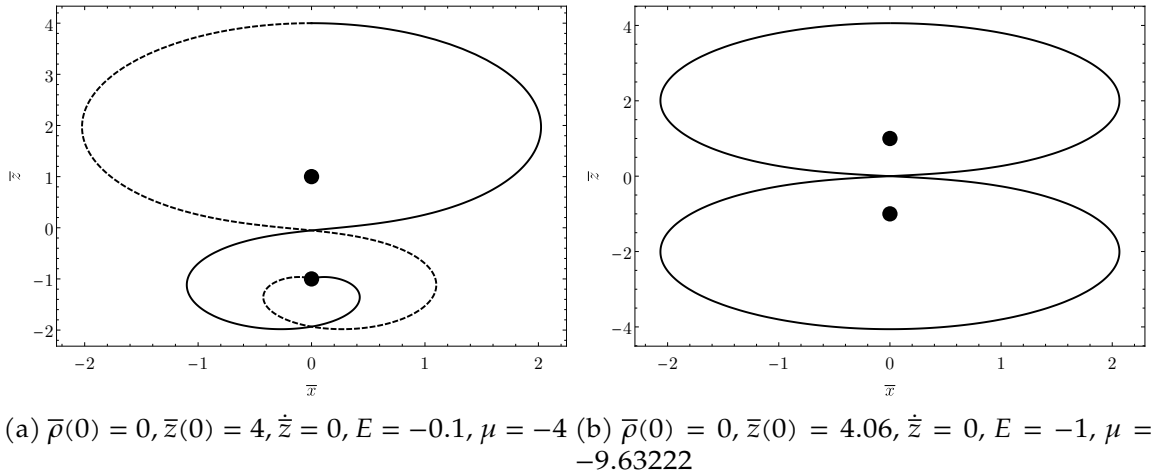
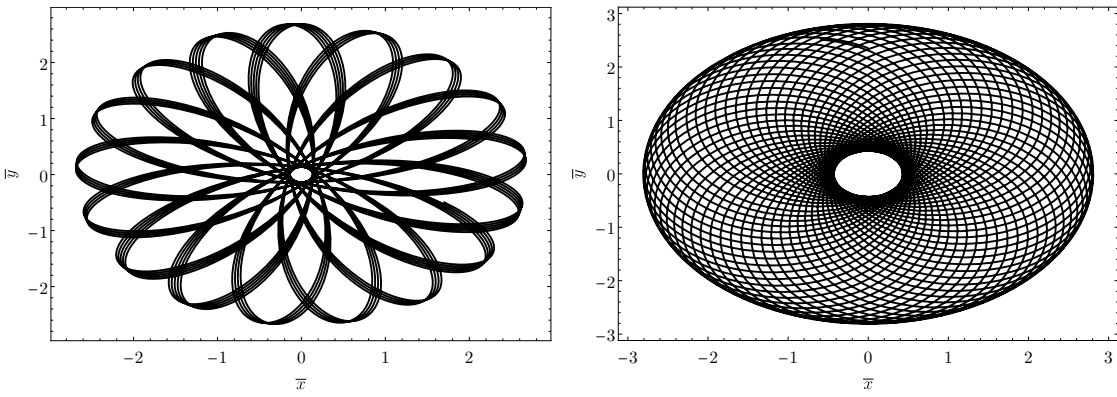


Figure 2.4: Two different types of orbits in the  $\rho$ - $z$  plane: terminating (left) and closed (right). Initial conditions used for each orbits are presented in their respective captions. The dashed trajectory represents that of negative  $\dot{\bar{\rho}}(0)$ .

motion we can now take full advantage of the effective potential formulation that we've introduced earlier. Our search revealed that particles with negative energy in this plane stay in a perpetual oscillatory motion either in straight lines or more complicated precessing orbits, depending on the value of  $L$ . These oscillating orbits are similar in nature to the closed orbits found in the  $\rho$ - $z$  plane as they also don't fall towards either of the black holes but they are stable in the sense that they do not require any fine tuning of the orbital parameters to be found, although they are globally unstable as any perturbation along the  $z$  direction will cause the to fall towards one of the black holes. Proceeding with the same rescaling by  $M_1$  scheme we've adopted so far, we plot in Figs. 2.5a and 2.5b two oscillating orbits for a binary system with  $M = \alpha = 1$ . Note that if an infinite amount of time is allowed to pass, a particle following these trajectories will have swept the whole finite area between the minimum and maximum values attained by  $\bar{\rho}$  during motion.

It's very hard (or even impossible) to obtain the orbital turning points of any oscillating orbit analytically by solving  $E_{\text{eff}}(\rho, 0)^2 - V_{\text{eff}}(\rho, 0) = 0$  for  $\rho$  as one can show that the problem reduces to finding the roots of a sixth-order polynomial equation. Despite that, it's quite easy to find the roots of the polynomial numeri-

cally after the orbital parameters have been chosen and thus this is the approach we've adopted as a complete and rigorous analysis of the orbital turning points go beyond the scope of this work. In Figs. 2.6a and 2.6b we plot the squared effective energy and the effective potential to the orbits described by 2.5a and 2.5b respectively and give their turning points. The effective potential is represented by a solid black line while the squared effective energy is represented by a dashed red line.



(a)  $\bar{\rho}(0) = 2$ ,  $\phi(0) = 0$ ,  $L = 2$ ,  $E = -1$  and (b)  $\bar{\rho}(0) = 2$ ,  $\phi(0) = 0$ ,  $L = 10$ ,  $E = -1$  and  $\mu = -6$ .

Figure 2.5: Two oscillating orbits in the  $z = 0$  symmetry plane. Note that the area swept by a particle in either orbit after an infinite amount of time is finite and proportional to the difference between the inner and outer orbital radii.

### 2.3.5 Examples of Penrose processes

Let us now give concrete examples of energy extraction in a binary black hole spacetime. As we've already seen, under a few different circumstances such as when the black holes are sufficiently apart, the charge-to-mass ratios of the fragments are sufficiently small or when the mass ratio is large, the ergosphere is composed by two disconnected regions. When this happens, the only way to extract energy from the binary is by having the negative energy trajectory reaching the event horizon of one of the black holes. Consequently, the negative energy particle will eventually reach one of the singularities. If, on the other hand, the black holes are sufficiently close to each other, an interesting

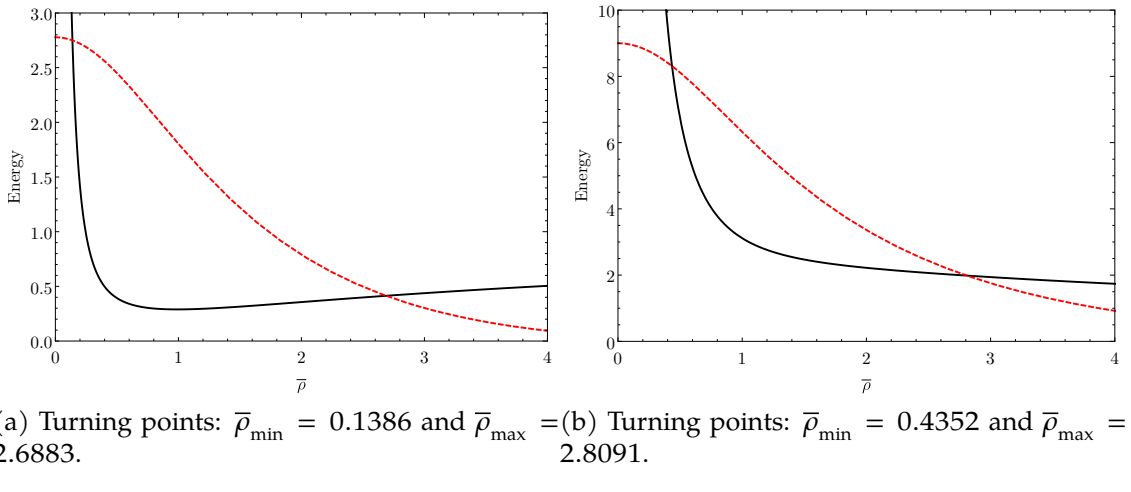


Figure 2.6: The effective potential (solid black line) and squared effective energy (dashed red line) for the orbits depicted in 2.5a (left) and 2.5b (right).

possibility opens up. Instead of having the negative energy orbit reach one of the event horizons, we can engineer the break up so that it will exist forever outside the black holes, confined to the ergosphere of the binary using trajectories like those in Figs. 2.4b, 2.5a or 2.5b. Naturally,  $T^{(1)}$  (the negative energy trajectory) will only make sense physically if  $\dot{\rho}^2 \geq 0$  everywhere. Thus, once  $E^{(1)}$  and  $L^{(1)}$  have been specified, the requirement that be non-negative constrains the possible value for the break-up coordinate  $\rho_0$ . Note that the angular break-up coordinate  $\phi_0$  is irrelevant due to the system being symmetric with respect to rotations around the  $z$  axis.

To construct an example, we start of by selecting a negative energy trajectory  $T^{(1)}$  and a break-up point inside the ergosphere. After that, we construct an arbitrary orbit of positive energy that reaches infinity to serve as  $T^{(2)}$ . By solving the system formed by Eqs. (2.14)-(2.17) together with the conservation of electric charge, one is able to determine all of the orbital parameters for  $T^{(0)}$ . In Table 2.1 we summarize the orbital parameters for the process depicted in Fig. 2.7. The particle comes in orbit  $T^{(1)}$  represented by the solid black curve and then splits at the grey dot into a negative energy orbit  $T^{(1)}$  represented by a blue dotted curve and a positive energy orbit  $T^{(2)}$  represented by a red dashed curve. In this example, we've set the spacetime parameters at  $M = \alpha = 1$  and

the two black dots represent the black hole's event horizons. Note that the entire process is confined to the  $\rho$ - $z$  plane.

Table 2.1: Orbital parameters for an example Penrose process in the  $\rho$ - $z$  plane.

$T^{(i)}$	$\mu^{(i)}$	$E^{(i)}$	$L^{(i)}$	$\rho_0^{(i)}$	$z_0^{(i)}$	$\dot{\rho}_0^{(i)}$	$\dot{z}_0^{(i)}$
$T^{(0)}$	0.16076	3.93401	0	0	4.06	3.82283	0
$T^{(1)}$	-9.63222	-1	0	0	4.06	-2.21869	0
$T^{(2)}$	10	10	0	0	4.06	6.52697	0

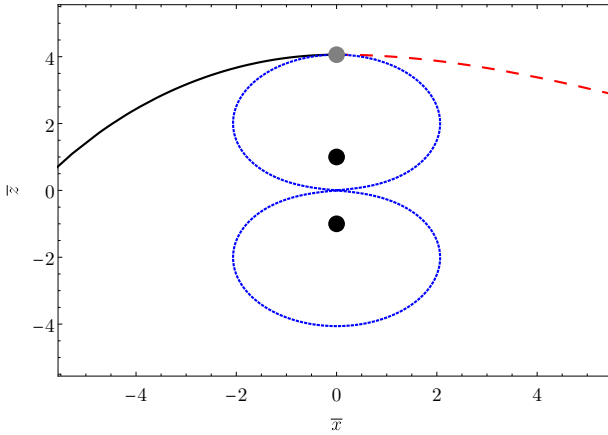


Figure 2.7: Example of a penrose process in the  $\rho$ - $z$  plane. The incoming trajectory (solid black) splits at the grey point into an negative energy (dotted blue) and increased energy (dashed red) orbit.

If instead we choose to confine our orbits to the  $z = 0$  plane, by employing the same algorithm with the same background spacetime parameters as before, we obtain the orbital parameters described in Tab. 2.2 and depicted in Fig. 2.8. Here we've chosen to draw only a few periods of the oscillating trajectory  $T^{(1)}$  to improve the figure's clarity.

Table 2.2: Orbital parameters for an example Penrose proces in the  $z = 0$  plane.

$T^{(i)}$	$\mu^{(i)}$	$E^{(i)}$	$L^{(i)}$	$\rho_0^{(i)}$	$z_0^{(i)}$	$\dot{\rho}_0^{(i)}$	$\dot{z}_0^{(i)}$
$T^{(0)}$	-0.85050	2.18701	1.70101	2	0	2.52301	0
$T^{(1)}$	-4	-1	2	2	0	-0.65820	0
$T^{(2)}$	0.5	10	4	2	0	-9.72474	0

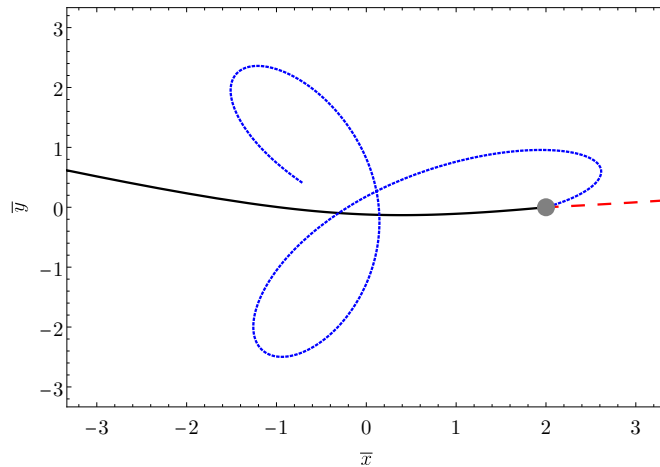


Figure 2.8: Example of a Penrose process that happens entirely on the  $z = 0$  plane of a MP binary black hole. Once again, the incoming trajectory (solid black) splits at the grey point into an negative energy (dotted blue) and increased energy (dashed red) orbit.

### 2.3.6 Efficiency of energy extraction

The efficiency  $\eta$  of the Penrose process can be trivially defined as the ratio between the energy input and output. Using Eq. (2.15), we can see that

$$\eta = -\frac{m^{(1)} E^{(1)}}{m^{(0)} E^{(0)}}. \quad (2.22)$$

One can choose  $E^{(1)} = 1$  and  $m^{(1)}/m^{(0)} = 1$  without any loss of generality. Furthermore it's clear that in order to obtain maximum efficiency, one must choose  $E^{(1)}$  to be as negative as possible, and thus of the form of Eq. (2.11). With these choices, the efficiency becomes

$$\eta = \mu^{(1)} \left( \frac{1}{U} - 1 \right) - \frac{1}{U}. \quad (2.23)$$

Notice that because (2.23) depends on  $U$ , the efficiency depends on the particle's position. Using spherical coordinates centered around the origin, one can see that as  $a \rightarrow 0$ ,

$$\eta = -\frac{\mu^{(1)}(M_1 + M_2) + r}{M_1 + M_2 + r}, \quad (2.24)$$

which is precisely the efficiency one would obtain for an extremal RN black hole of mass  $M_1 + M_2$  in a coordinate system where the event horizon is a point. If the particle is located precisely at the event horizon, and thus  $r = 0$ , the efficiency attains its maximum value of  $-\mu^{(1)}$ . The direct consequence of this fact is that one can have Penrose processes in which the efficiency of energy extraction goes above 100% (as  $\mu^{(1)}$  can be arbitrarily large) if the participating particles are electrically charged, a well known fact pointed out in Refs. [48] and [49].

Additionally, because  $0 \leq 1/U \leq 1$ , one can easily see from Eq. (2.23) that  $0 \leq \eta \leq -\mu^{(1)}$  and thus the presence of the second black hole does not allow for more efficient processes than the single RN black hole. It's also noteworthy that  $\eta$  attains its maximum value when  $1/U = 0$  which occurs only when the particle is exactly over one of the event horizons. In Fig. 2.9, we plot the extraction efficiency for a MP binary with mass ratio  $M = 1$  and varying separation parameter  $\alpha$  for a particle of charge-to-mass ratio  $\mu = -1$  located at  $\bar{r} = 1$  and  $\bar{\theta} = 0$  (solid black line),  $\bar{\theta} = \pi/8$  (dashed red line) and  $\bar{\theta} = \pi/2$  (dotted blue line). The maximum value of  $\alpha$  is capped by the generalized ergosphere condition of Eq.(2.13). Note that the maximum efficiency of  $-\mu = 2$  is attainable only when the particle is located at one of the event horizons, namely when  $\alpha = 1$  and  $\bar{\theta} = 0, \pi/2$ .

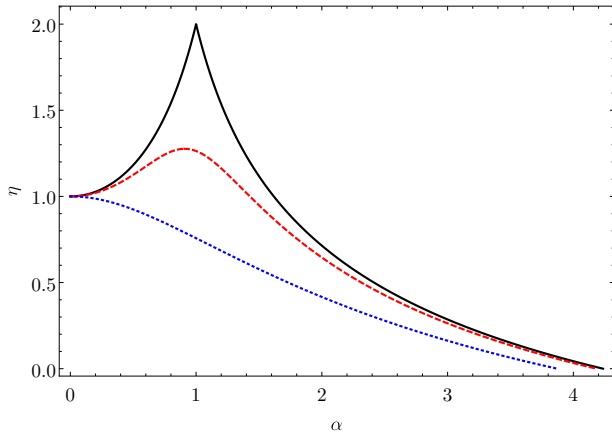


Figure 2.9: Extraction efficiency for a particle  $\bar{r} = 1$  and  $\bar{\theta} = 0$  (solid black line),  $\bar{\theta} = \pi/8$  (dashed red line) and  $\bar{\theta} = \pi/2$  (dotted blue line). Maximum efficiency is attained at  $\alpha = 1$  and  $\bar{\theta} = 0, \pi/2$ .

## 2.4 CMMR Spacetime

## 2.5 CMMR spacetime

We will now perform an analysis similar to that of the previous section but using the solution class found by Cabrera-Munguia, Manko and Ruiz (CMMR). This metric describes a pair of static Kerr black holes and thus we will show that one can extract rotational energy from the system using geodesic motion.

### 2.5.1 Spacetime metric

In Weyl's cylindrical coordinates, the CMMR line element reads

$$ds^2 = -f(\rho, z) [dt - \omega(\rho, z)d\varphi]^2 + f(\rho, z)^{-1} [e^{2\gamma(\rho, z)} (d\rho^2 + dz^2) + \rho^2 d\varphi^2] \quad (2.25)$$

where the real valued functions  $f(\rho, z)$ ,  $\omega(\rho, z)$  and  $\exp[2\gamma(\rho, z)]$  were implemented as described in Sec. IV of Ref. [15]. We shall not reproduce these functions here as they take a few pages worth of equations.

This solution is characterized by a set five parameters: The masses of the Kerr constituents  $m_1$  and  $m_2$ , their angular momenta per unit mass  $a_1$  and  $a_2$  and the coordinate distance between the centers of the two black holes  $R$ . In Weyl's coordinates, each horizon is a line that extends over the  $z$  axis centered around  $z = \pm R/2$  (See Fig. 3 of Ref. [15]). In order to work with dimensionless quantities, we will introduce the three additional parameters given in terms of the preceding five. The first is the total mass of the system  $M$ , given by

$$M = m_1 + m_2. \quad (2.26)$$

The second is the system's mass ratio  $q$  given by

$$q = \frac{m_1}{m_2} \quad (2.27)$$

and finally, the third is a dimensionless distance parameter  $b$  given by

$$b = \frac{M}{R}. \quad (2.28)$$

By performing the coordinate transformation

$$x^\mu \rightarrow \frac{x^\mu}{M} \quad (2.29)$$

where the  $x^\mu$  are the space-time coordinates, we effectively rescale the metric functions  $f$ ,  $\omega$  and  $e^{2\gamma}$  by a factor of  $1/M$  and as a result they become dimensionless quantities with the added benefit that the space-time coordinates  $t$ ,  $\rho$ ,  $z$  and  $\varphi$  are also dimensionless quantities.

If additionally we fixate  $M$  to be unitary, we can fully describe the CMMR metric by specifying four dimensionless parameters  $q$ ,  $b$ ,  $a_1$  and  $a_2$  from which all necessary quantities appearing in the metric functions can be calculated. Explicitly, we can write the inverse relations

$$m_1 = \frac{Mq}{1+q}, \quad (2.30)$$

$$m_2 = \frac{M}{1+q} \quad (2.31)$$

and

$$R = \frac{M}{b}. \quad (2.32)$$

The CMMR solution when written in the form given by Ref. [15] can appropriately describe not only a “standard” Kerr black hole binary but also extreme and naked Kerr sources, depending on the values chosen for the solution’s parameters. In order to study scenarios of greater astrophysical relevance we shall limit ourselves to discussions pertaining only to the black hole sector of the metric which is given by the set of parameters that cause the constituent black holes horizons half lengths (the expressions for  $\sigma_1$  and  $\sigma_2$  after Eq. (18) of Ref. [15]) to be real valued and greater than zero. By choosing values of  $q$  and  $b$ , we are able to determine which values of  $a_1$  and  $a_2$  represent black hole binary solutions. The results are presented in Fig. 2.10. For each  $q$  and  $b$  pair, a blue shape

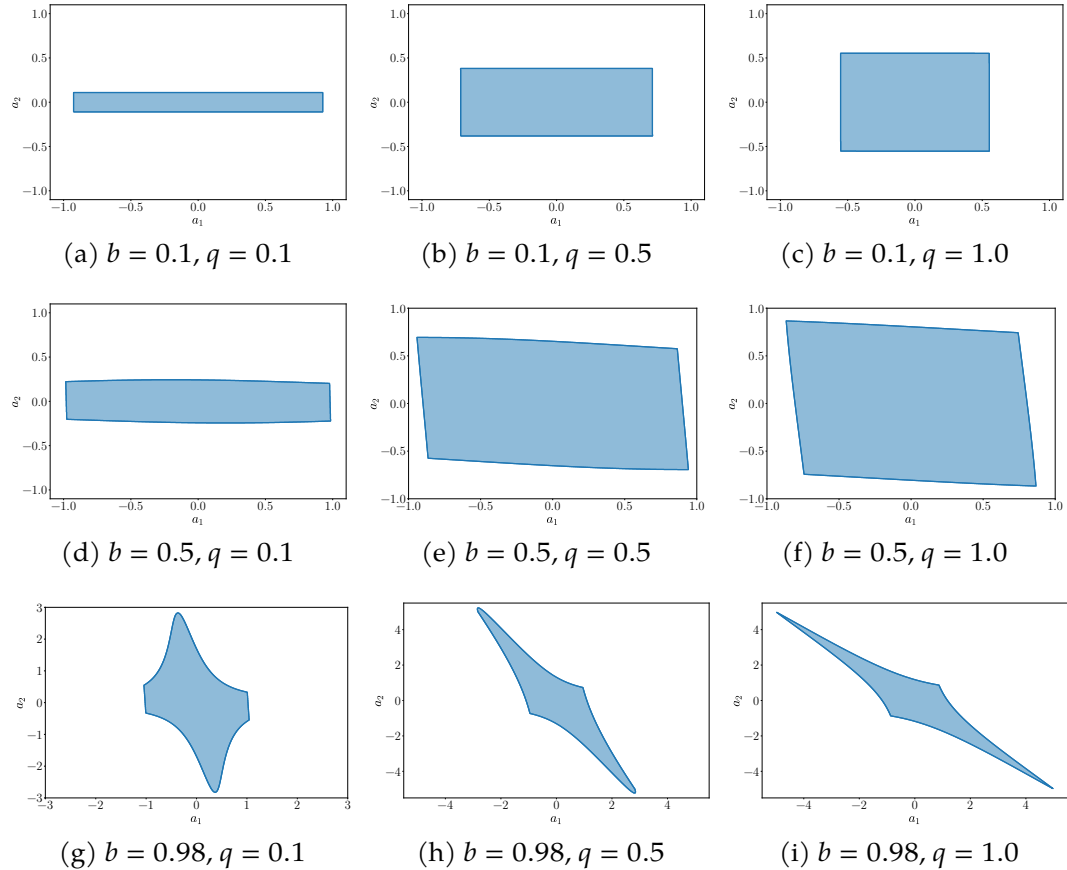


Figure 2.10: Parameter space variations in the CMMR solution. All  $a_1$  and  $a_2$  values inside of the blue region represent a valid black hole binary solution for a set of indicated  $q$  and  $b$  values.

represents the region of  $a_1$  and  $a_2$  values representing black hole configurations.

## 2.5.2 Ergospheres

In the context of stationary space-times the ergosphere is defined as the region in which observers can no longer be static and are “dragged” along the space-time’s rotation. More precisely it is the region in which the time translation Killing vector field  $K = \partial_t$  becomes space-like, that is,  $g_{\mu\nu}K^\mu K^\nu > 0$  [37]. In the specific case of the CMMR metric, by employing Eq. (2.25) we see that the

ergosphere is the locus of all points  $(\rho, z)$  that satisfy

$$f(\rho, z) < 0. \quad (2.33)$$

Given the complexity of  $f(\rho, z)$  it is extremely difficult (or even impossible) to find an explicit expression for  $\rho$  and  $z$  that satisfy Eq. (2.33) thus we will visualize the ergospheres and their features in the CMMR solution numerically. Knowing that the relation between Weyl's radial coordinate  $\rho$  and Cartesian coordinates  $x$  and  $y$  are  $x = \rho \cos \varphi$  and  $y = \rho \sin \varphi$  we can project and plot  $f(\rho, z)$  in the  $x$ - $z$  plane by choosing  $\varphi = 0$ .

To create the plots, we have fixed  $q = 1.0$  and  $|a_{1,2}| = 0.65$  while gradually increased  $b$  from 0.3 to 0.98. This allows us to view the ergosphere around each constituent of the binary changing as their mutual interaction grows stronger. In Fig. 2.11 we show the variation of the ergosphere for constituents of aligned spins and in Fig. 2.12 for constituents with anti-aligned spins. In all of the figures the ergosphere is the light blue region, bounded by the darker blue line and the event horizons are black lines. In both cases, the ergospheres start localized around each black hole. The choice of parameters in the figures intentionally lead to horizons that are initially very short which means that the black hole are spinning close to extremality.

Let us now focus on Fig. 2.11. As the holes get closer, the familiar “infinity shaped” ergosphere around each hole starts to deform in a very particular way: both of the tips of each ergosphere start to bend towards the other until they touch and eventually form a larger region that encompasses both holes and. Even more interesting, as the system gets closer to merging, the event horizons themselves get “stretched” along the  $z$  direction. It becomes clear that in this case the ergospheres and event horizons “add up” to create structures larger than the originals.

Switching focus to Fig. 2.12 that in spite of the fact that the event horizons still “stretch” what appears to be the opposite of the aligned spin case happens for the ergospheres. Instead of bending towards each other they are repelled to the point that when they are close to merging, their shape becomes very thin and elongated. In other words, the ergospheres become *spaghettified* and “can-

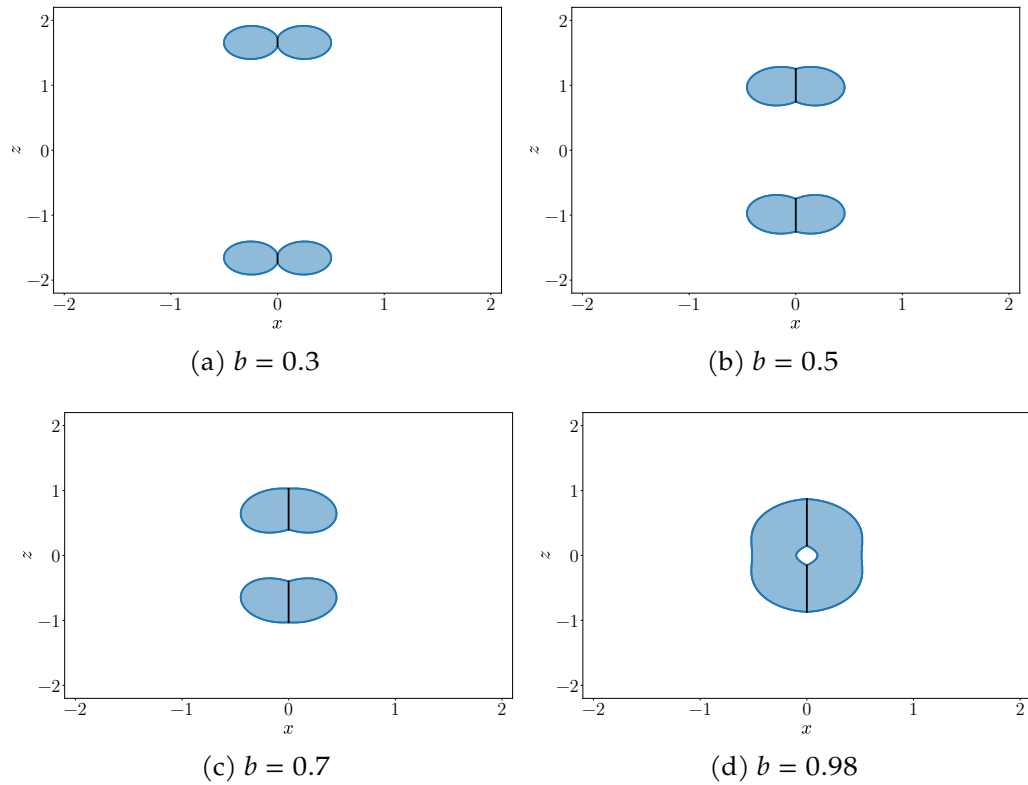


Figure 2.11: Ergosphere of a binary Kerr black hole system with mass ratio  $q = 1.0$  and aligned spins  $a_1 = 0.65$  and  $a_2 = 0.65$  for different separation parameters. The blue region represents the ergosphere while the black lines represent the event horizons.

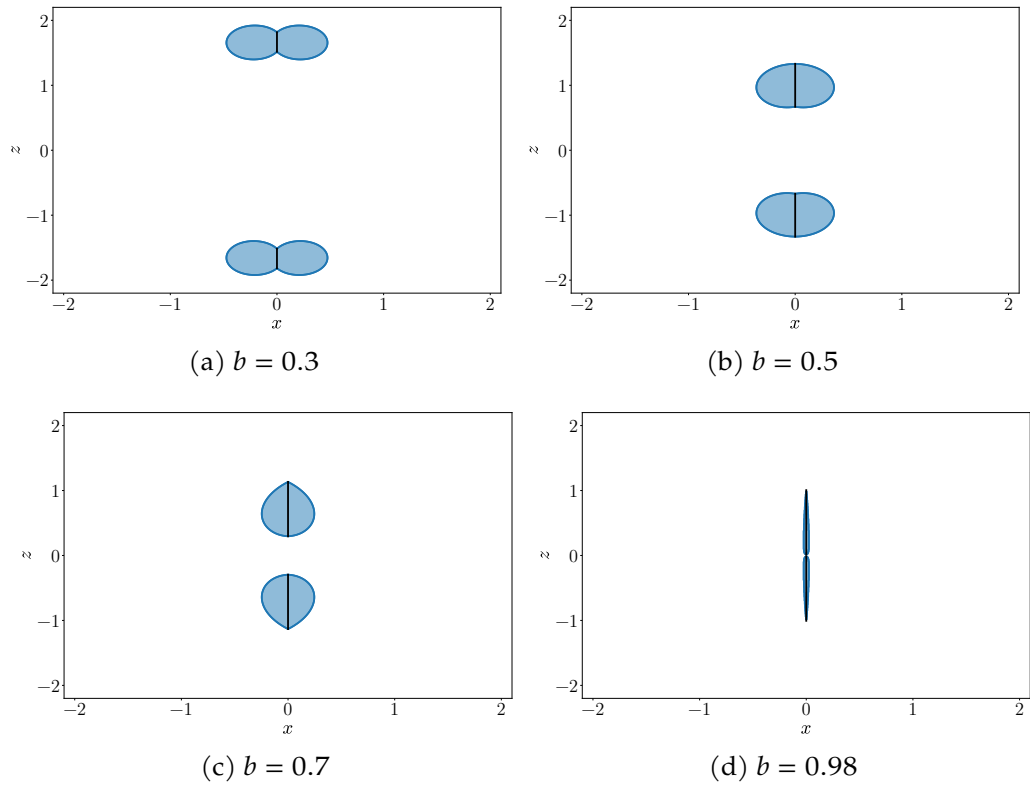


Figure 2.12: Ergosphere of a binary Kerr black hole system with mass ratio  $q = 1.0$  and aligned spins  $a_1 = 0.65$  and  $a_2 = 0.65$  for different separation parameters. The blue region represents the ergosphere while the black lines represent the event horizons.

cel out" in the case of equal but anti-aligned spins.

These results are not physically surprising. One expects that black holes that have exactly the same spin but in opposite directions when merged create a resulting black hole that has more mass but no spin, that is, their counter rotation balances and cancels out. The opposite is expected to happen for black holes with aligned spins: both their masses and angular momenta are added up upon merging. The novelty of our work is, we believe, in the fact that even using an analytic solution containing an unphysical strut that keeps the black holes from colliding such features are apparent and can be demonstrated with relative ease.

Now that the general shapes and features of the ergospheres have been established, we can ask ourselves how far apart should the Kerr black holes be so that their individual ergospheres merge into one? From Fig. 2.12 we can see that if the spins are exactly equal in modulus but differ in sign such merging is impossible. Nevertheless, from Fig. 2.11 we see that when the spins are equal we can be sure that such merging occurs for some value of  $b$ . It is not unreasonable to imagine that in the intermediary case is considered, that is anti-aligned spins that are not exactly equal, such merging also occurs.

In order to visualize the parameter regions that are able to produce connected ergospheres we plot the regions for which the parameters produce physical black hole binarys (i.e., black holes and not naked singularities) and  $f(\rho, 0) = 0$  for some value of  $\rho$ . These are the blue regions shown in Fig. 2.13 where we increased  $b$  from 0.89 to 0.98 while also increasing the mass ratio from 0.1 to 1.0 and in Fig. 2.14 where  $a_1$  and  $q$  were fixed but  $a_2$  and  $b$  were allowed to change instead. It is extremely important to point out that despite what the figures indicate the configuration  $a_1 = a_2 = 0$  does not produce an ergosphere. These points are included in our graphs but should be disregarded as the CMMR solution in the form presented in Ref. [15] (which is the source of all metric quantities used in this work) does not describe the black hole system correctly if one of the spins is zero. This case must be treated separately and is discussed in detail in Ref. [14].

Let us now focus on Fig. 2.13. For any given mass ratio, it is apparent that the increase in the distance parameter increases the overall size of the parameter

region producing joint ergospheres. The most interesting feature is that certain configurations of equal but opposite spins can also produce a joined ergosphere if the masses are not equal. This can be easily seen in Fig. 2.13e if  $a_1 = 0.5$  and  $a_2 = -0.5$ .

In Fig. 2.14 we look at the influence of the distance parameter in more detail. The first apparent feature is that for equal mass binaries, the configuration where  $a_2 = -a_1$  never produces a joined ergosphere, even for very large distance parameters (and thus very small distances). This can easily be seen in Fig. 2.14b and Fig. 2.14d. We can also observe that for a fixed mas ratio, an increase in the fixed spin parameter  $a_1$  causes the area of the graph to become larger in the negative region of  $a_2$  which can be seen in Fig. 2.14a and Fig. 2.14c. This indicates that for binaries with unequal masses, configurations with opposite spins can generate joined ergospheres more easily. Furthermore we can observe the universal need of  $b$  being large in order to create joined ergospheres.

### 2.5.3 Geodesic motion in the $z = 0$ plane

We will make use of the Lagrangian formalism to determine the form of the geodesic equations and the motion's conserved quantities. Letting a dot represent derivatives with respect to the proper time we can write the Lagrangian of the geodesic motion as [37]

$$2\mathcal{L} = -f(\dot{t} - \omega\dot{\phi})^2 + f^{-1} [e^{2\gamma} (\dot{\rho}^2 + \dot{z}^2) + \rho^2\dot{\phi}^2]. \quad (2.34)$$

From Eq. (2.34) we can identify two constants of the motion, the energy per unit mass as measured by a static observer at infinity  $E$ , given by

$$E = f\dot{t} - \omega f\dot{\phi} \quad (2.35)$$

and the angular momentum about the  $z$  axis per unit mass as measured by a static observer at infinity  $L$ , given by

$$L = \omega f\dot{t} + \left( \frac{\rho^2}{f} - \omega^2 f \right) \dot{\phi}. \quad (2.36)$$

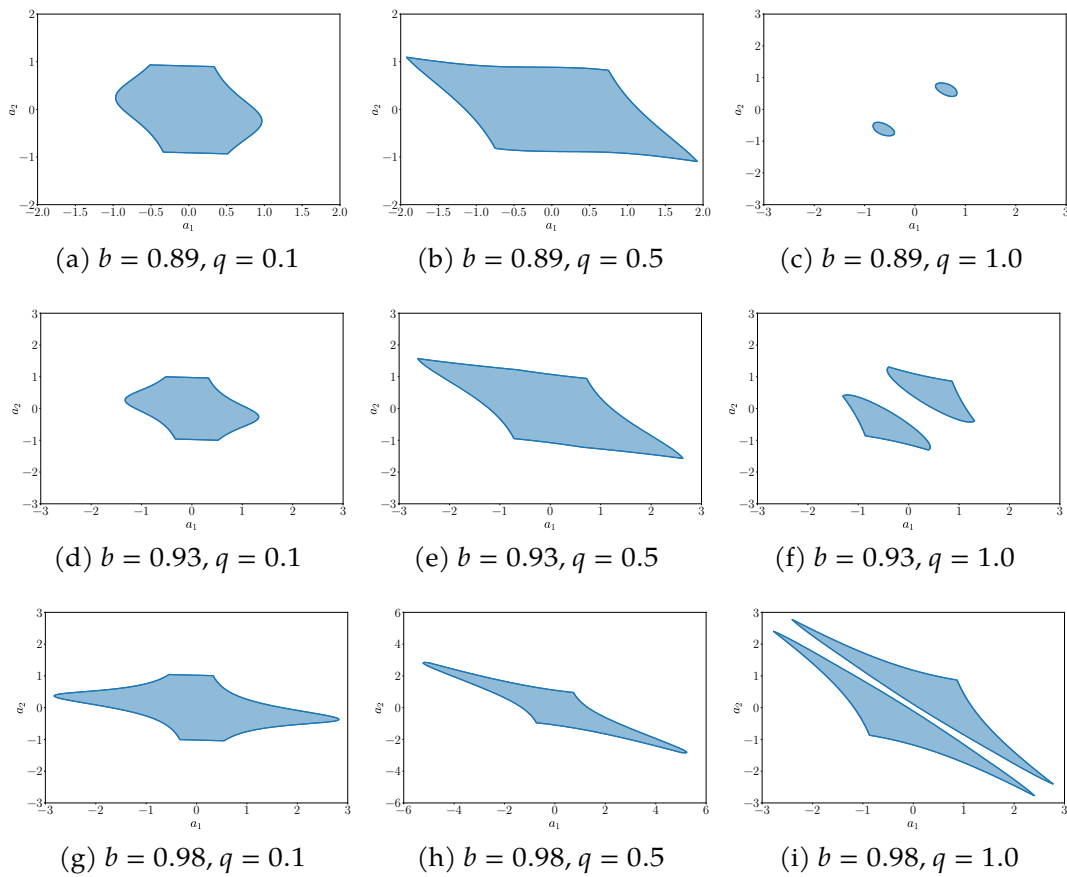


Figure 2.13: Parameter spaces that allow for a common ergosphere. The blue regions represent pairs of  $a_1$  and  $a_2$  values that produce an ergosphere around both black holes for each  $(b, q)$  indicated value.

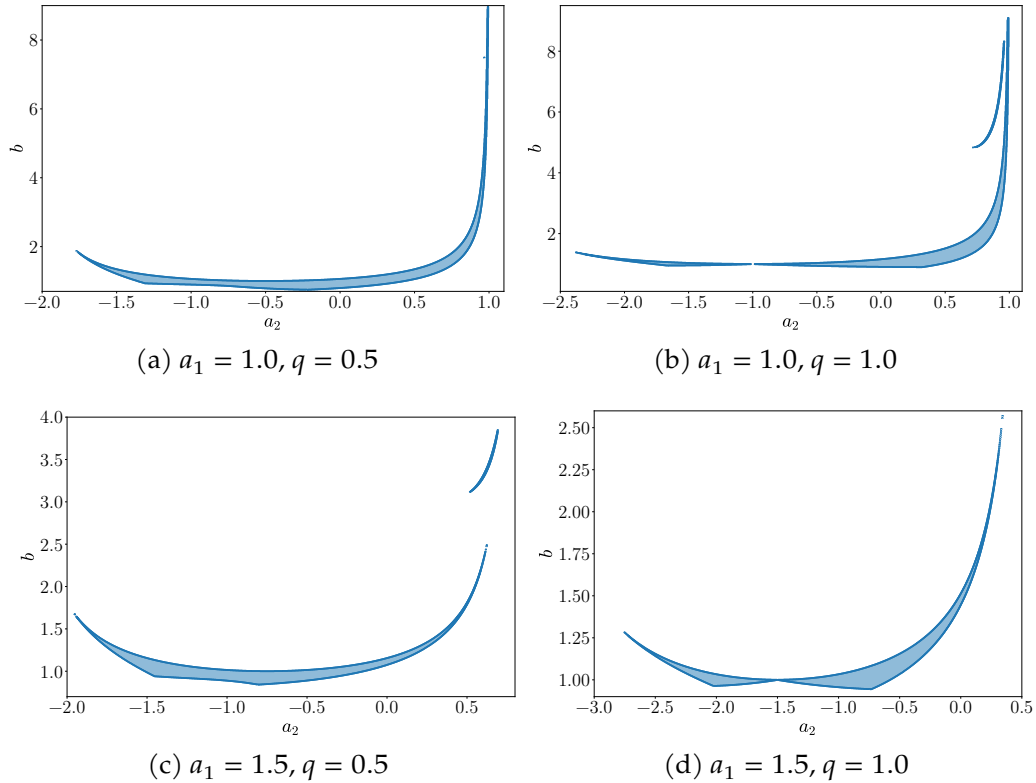


Figure 2.14: Parameter spaces that allow for a common ergosphere. The blue regions represent pairs of  $b$  and  $a_2$  values that produce an ergosphere around both black holes for each  $(a_1, q)$  indicated value.

We can use Eqs. (2.35) and (2.36) to find  $\dot{t}$  and  $\dot{\phi}$ , in terms of  $E$  and  $L$  which yield

$$\dot{t} = \frac{E}{f} + \frac{\omega f(L - E\omega)}{\rho^2} \quad (2.37)$$

and

$$\dot{\phi} = \frac{f(L - E\omega)}{\rho^2} \quad (2.38)$$

A third conserved quantity is the normalization of the four velocity for a massive particle, that is,  $g_{\mu\nu}\dot{x}^\mu\dot{x}^\nu = -1$  which can be combined with Eqs. (2.37) and (2.38) to produce an expression for the particle's energy in terms of its "spatial" four velocities ( $\dot{\rho}$  and  $\dot{z}$ ) and it's angular momentum  $L$ , yielding

$$E = \frac{-f^2\omega L}{\rho^2 - \omega^2 f^2} + \left[ \frac{\rho^2 e^{2\gamma}(\dot{\rho}^2 + \dot{z}^2)}{\rho^2 - \omega^2 f^2} + \left( \frac{\rho f L}{\rho^2 - \omega^2 f^2} \right)^2 + \frac{\rho^2 f}{\rho^2 - \omega^2 f^2} \right]^{1/2} \quad (2.39)$$

where the positive sign is chosen for the square root to guarantee that a static particle at infinity has positive energy.

By inverting Eq. (2.39) to obtain  $\dot{\rho}^2 + \dot{z}^2$  we are motivated to define the effective potential

$$V_{\text{eff}} = \frac{\rho^2 - \omega^2 f^2}{\rho^2 e^{2\gamma}} \left[ \left( \frac{\rho f L}{\rho^2 - \omega^2 f^2} \right)^2 + \frac{\rho^2 f}{\rho^2 - \omega^2 f^2} \right] \quad (2.40)$$

and the effective energy

$$E_{\text{eff}} = \frac{\rho^2 - \omega^2 f^2}{\rho^2 e^{2\gamma}} \left( E + \frac{f^2 \omega L}{\rho^2 - \omega^2 f^2} \right)^2 \quad (2.41)$$

and therefore we can write

$$\dot{\rho}^2 + \dot{z}^2 = E_{\text{eff}} - V_{\text{eff}}. \quad (2.42)$$

Finally, the geodesic equations can be derived using the Euler-Lagrange equa-

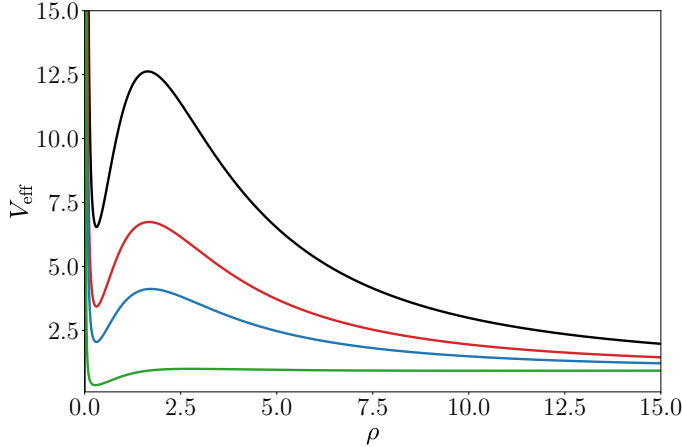


Figure 2.15: Effective potential in the  $z = 0$  plane for  $L = 18, 13, 10$  and  $4$  (black, red, blue and green curves respectively).

tions for the Lagrangian of Eq. (2.34) and  $t$  and  $\dot{\phi}$  can be replaced with Eqs. (2.37) and (2.38), respectively. While studying geodesic motion in binary system of two identical Kerr-Newman black holes held by a massless strut (a solution with the same general line element as Eq. (2.25)) the authors of Ref. [50] in Eqs. (16) and (17) derive the explicit form of the geodesic equations for  $\rho$  and  $z$  in terms of  $E$ ,  $L$  and the metric functions  $f$ ,  $\omega$  and  $e^{2\gamma}$  and thus we shall not repeat this information here. In our work, whenever was necessary to solve the geodesic equations numerically we implemented Eqs. (16) and (17) of Ref. [50] directly, changing only the metric functions to those described in Sec. IV of Ref. [15].

If the motion is constrained to the  $z = 0$  symmetry plane, we can easily determine the general characteristics of massive particle geodesics by plotting the effective potential, Eq. (2.40), as was done in Fig. 2.15. The different curves represent different values of angular momenta, specifically  $L = 18$  in the black curve,  $L = 13$  in the red curve,  $L = 10$  in the blue curve and  $L = 4$  in the green curve. We can see that both stable and unstable circular orbits are possible, as well as escaping orbits and non-circular bounded orbits that become “wider” as the value of  $L$  decreases.

### 2.5.4 Negative energy orbits

Now we turn our attention to the conditions required for a orbit to have negative energy for a static observer at infinity, as this is a necessary condition for the occurrence of the Penrose process. By inspecting Eq. (2.39) we can immediately conclude that since the term in the square root is always positive, a necessary (but not sufficient) condition for the particle's energy to be negative is that

$$\frac{-f^2\omega L}{\rho^2 - \omega^2 f^2} < 0. \quad (2.43)$$

Multiplying both sides by the denominator we conclude that the numerator must be negative. Because  $-f^2$  is always negative, the necessary condition for the existence of negative energy orbits is that

$$(\omega < 0 \wedge L > 0) \vee (\omega > 0 \wedge L < 0) \quad (2.44)$$

which simply means that the horizons must rotate in the opposite direction of the particles own rotation.

Despite  $\omega(\rho, z)$  being known analytically, its complexity does not allow us to easily reason about its behaviour and thus we proceeded to visualize it numerically employing the same projection scheme in the Cartesian plane as was done in the visualisation of the ergosphere. With that we obtain Fig. 2.16. The color indicates the value of  $\omega$  at each point  $(x, y)$  and the values that were graphed were deliberately chosen to lie in the range  $-25 \leq \omega \leq 25$  in order to facilitate the visualization. In all panels we choose  $b = 0.98$  and  $q = 1.0$ . The upper left panel shows a configuration with aligned spins  $a_1 = a_2 = 0.65$  and the upper right shows the equivalent configuration with anti-aligned spins  $-a_1 = a_2 = 0.65$ . The lower row shows binaries with anti-aligned but very different spins with  $a_1 = 0.65$  and  $a_2 = -0.1$  in the left panel and  $a_1 = -0.65$  and  $a_2 = 0.1$  in the right panel. In all cases the green curve marks the boundary of the ergosphere and the black lines mark the event horizons.

From Fig. 2.16 it becomes clear that in the case of a system with aligned or anti aligned but very different spins one can extract energy from either of the two black holes by setting the sign of  $L$  to be opposite to that of  $\omega$  inside the

ergosphere. The black hole that will ultimately loose part of it's energy can then only be determined uniquely from the other dynamical parameters of the particle's trajectory. In the case of anti-aligned but equal or similar spins the sign of  $L$  determines uniquely which black hole can be used for energy extraction, which will be either the upper or lower black hole, depending on the sign configurations of  $\omega$  and  $L$  inside the ergosphere. This feature is completely compatible with the notion that energy can only be extracted inside the ergosphere. For spin configurations in which a single ergosphere exists around both black holes, energy can be extracted from either hole while in configurations in which the ergospheres are located around each hole but are disconnected, energy can be extracted from only one of the constituents.

### 2.5.5 Efficiency of energy extraction

We now turn our attention to the maximum energy that can be extracted from the system by means of the Penrose process. It widely known that no more energy can be extracted than the *irreducible mass* of each black hole [32, 41, 37]. The irreducible mass  $M_{\text{irr}}$  is related to the horizon area  $A$  by the well known formula [37]

$$M_{\text{irr}} = \sqrt{\frac{A}{16\pi}}. \quad (2.45)$$

The entropies of each black hole in the CMMR metric are known and given in Eq. (22) of Ref. [15]. Given that the entropy  $S$  and horizon area are related by  $A = 4S$  we have that the maximum energy that can be extracted from the system is the sum of the maximum energy that can be extracted from each hole individually, that is

$$E_{\text{max}} = \left( m_1 - \sqrt{\frac{S_1}{4\pi}} \right) + \left( m_2 - \sqrt{\frac{S_2}{4\pi}} \right). \quad (2.46)$$

In the traditional Penrose process there is only one particle of negative energy and thus only one of the black holes will loose part of its rotation. In practice this means that only one of the terms inside the parenthesis of Eq. 2.46 will contribute to the energy extraction. A remarkable fact is that if one takes

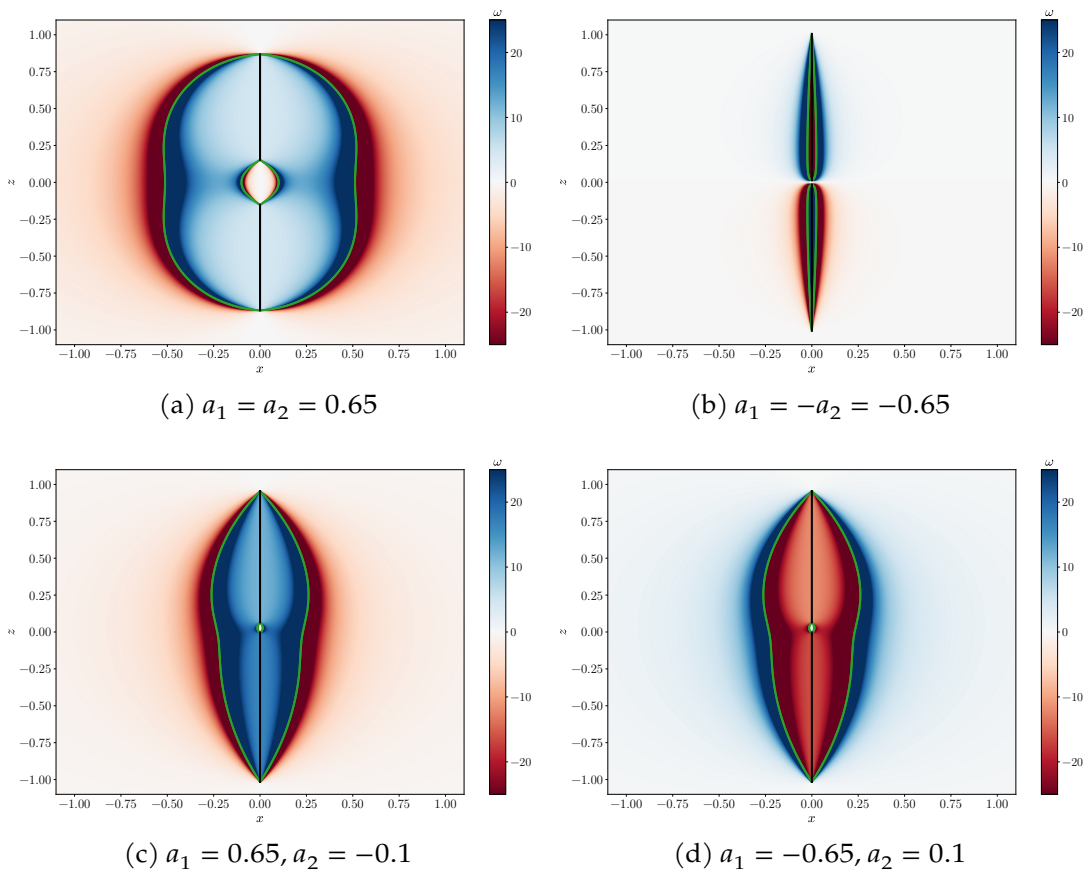


Figure 2.16: The value of  $\omega(\rho, z)$  projected in Cartesian coordinates. In all plots  $b = 0.95$  and  $q = 1.0$ . The green curve marks the limit of the ergosphere and the black lines mark the event horizons.

the limit of  $R \rightarrow \infty$  of one of these terms (e.g. the first) in Eq. 2.46 one obtains

$$E_{\max} = m_1 - \frac{1}{\sqrt{2}} \left( m_1^2 + \sqrt{m_1^4 - j_1^2} \right)^{1/2} \quad (2.47)$$

where we remind that  $j_1 = a_1 m_1$ . This expression is exactly the one obtained for the maximum extracted energy in the case of a single Kerr black hole of mass  $m_1$  and angular momentum  $j_1$  [37] which reassures us to the fact that a Kerr binary behaves as a system of isolated Kerr black holes if their separation is large.

## 2.6 Geodesic motion in arbitrary space-times

In this section we will discuss a method that we intend to implement which would allow us to investigate the Penrose process in arbitrary (even numerically evolved) spacetimes. As we've seen, the Penrose mechanism depends on the existence of orbits that have negative energy according to a static observer far away from the system. If such orbits exist, energy can be extracted from the system. We've also shown that such orbits must lie inside the ergosphere of the binary system, but the notion of ergosphere is not easily generalized to dynamic space-times and remains an open problem. Instead of attempting to define an ergosphere in a dynamical background, we will investigate geodesic motion in such background. The methods and tools for this are already well known in the branch of *ray tracing* in NR for computing the shadows of binary black holes. It all hinges on the ADM (Arnowitt, Deser and Misner) of the geodesic equation.

### 2.6.1 ADM Decomposition of the geodesic equation

The ADM decomposition, also known as the  $3 + 1$  decomposition is a formulation of GR that rewrite Einstein's field equations as a Cauchy (initial value) problem and is a very common representation of spacetimes used in NR. In this decomposition, the spacetime metric is written as [51]

$$ds^2 = -\alpha^2 dt^2 + \gamma_{ij} (dx^i + \beta^i dt) (dx^j + \beta^j dt) \quad (2.48)$$

where  $\alpha$  is the lapse function,  $\beta^i$  the shift vector and  $\gamma_{ij}$  the spatial metric.

The decomposition of the geodesic equation we will adopt follows Ref. [52] closely. We note that a very similar approach was also developed in Ref. [53], which we also refer to for additional details. We start by defining the auxiliary variable

$$\Pi_i \equiv \frac{p_i}{\alpha p_0} = \frac{p_i}{\sqrt{\gamma^{jk} p_j p_k}} \quad (2.49)$$

where  $p^i \equiv dx^i/d\tau$  is the particle's 4-momentum,  $x^i$  the spacetime coordinates and  $\tau$  the particle's proper time.

Using the ADM decomposition, the geodesic equation can be written as [52]

$$\frac{d\Pi_i}{dt} = -\partial_i \alpha + \left[ (\partial_j \alpha) \Pi^j - \alpha K_{jk} \Pi^j \Pi^k \right] \Pi_i + (\partial_i \beta^k) \Pi_k - \frac{1}{2} \alpha (\partial_i \gamma^{jk}) \Pi_j \Pi_k \quad (2.50)$$

$$\frac{dx^i}{dt} = \alpha \Pi^i - \beta^i \quad (2.51)$$

$$\frac{d \ln(\alpha p^0)}{dt} = -(\partial_i \alpha) \Pi^i + \alpha K_{ij} \Pi^i \Pi^j \quad (2.52)$$

where  $t$  is the coordinate time,  $K_{ij}$  is the extrinsic curvature and  $\Pi^i = \gamma^{ij} \Pi_j$ .

## 2.6.2 Observed quantities

## 2.6.3 Proposal for investigating the Penrose process in numeric space-times

# 2.7 Arbitrary Spacetimes

Arbitrary Penrose



# **Chapter 3**

## **Numerical Scalar Wave Scattering in GW150914**



# **Chapter 4**

## **Conclusions and perspectives**

CONCLUSION



# Bibliography

- [1] R. A. Hulse and J. H. Taylor, *Astrophys. J.* **195**, L51 (1975).
- [2] B. P. Abbott *et al.* (Virgo, LIGO Scientific), *Phys. Rev. Lett.* **116**, 061102 (2016), arXiv:1602.03837 [gr-qc].
- [3] E. Berti, *APS Physics* **9**, 17 (2016), arXiv:1602.04476 [gr-qc].
- [4] G. W. Gibbons, *Comm. Math. Phys.* **44**, 245 (1975).
- [5] P. T. Chruściel, J. L. Costa, and M. Heusler, *Living Reviews in Relativity* **15**, 7 (2012).
- [6] N. Gürlebeck, *Phys. Rev. Lett.* **114**, 151102 (2015).
- [7] S. D. Majumdar, *Phys. Rev.* **72**, 390 (1947).
- [8] A. Papapetrou, *Proc. Roy. Irish Acad. (Sect. A)* **51**, 191 (1947).
- [9] J. B. Hartle and S. W. Hawking, *Comm. Math. Phys.* **26**, 87 (1972).
- [10] D. Bini, A. Geralico, G. Gionti, S. J., W. Plastino, and N. Velandia, *Gen. Rel. Grav.* **51**, 153 (2019), arXiv:1906.01991 [gr-qc].
- [11] W. Israel and G. A. Wilson, *Journal of Mathematical Physics* **13**, 865 (1972).
- [12] Z. Perjés, *Physical Review Letters* **27**, 1668 (1971).
- [13] I. Cabrera-Munguia, *Physics Letters B* **786**, 466 (2018).
- [14] V. Manko and E. Ruiz, *Physics Letters B* **794**, 36 (2019).

## BIBLIOGRAPHY

---

- [15] C. J. Ramírez-Valdez, H. García-Compeán, and V. S. Manko, *Phys. Rev. D* **102**, 024084 (2020).
- [16] P. V. Cunha, C. A. Herdeiro, and M. J. Rodriguez, *Physical Review D* **98**, 10.1103/physrevd.98.044053 (2018).
- [17] P. V. Cunha, C. A. Herdeiro, and M. J. Rodriguez, *Physical Review D* **97**, 10.1103/physrevd.97.084020 (2018).
- [18] M. Visser, in *Kerr Fest: Black Holes in Astrophysics, General Relativity and Quantum Gravity* (2007) arXiv:0706.0622 [gr-qc].
- [19] C. Bambi, *Mod. Phys. Lett. A* **26**, 2453 (2011), arXiv:1109.4256 [gr-qc].
- [20] S. A. Teukolsky, *Class. Quant. Grav.* **32**, 124006 (2015), arXiv:1410.2130 [gr-qc].
- [21] E. Berti, *Gen. Rel. Grav.* **51**, 140 (2019), arXiv:1911.00541 [gr-qc].
- [22] R. Penrose and R. M. Floyd, *Nature Physical Science* **229**, 177 (1971).
- [23] J. D. Schnittman, *Gen. Rel. Grav.* **50**, 77 (2018), arXiv:1910.02800 [astro-ph.HE].
- [24] S. M. Wagh, S. V. Dhurandhar, and N. Dadhich, *The Astrophysical Journal* **290**, 12 (1985).
- [25] A. Tursunov and N. Dadhich, *Universe* **5**, 125 (2019), arXiv:1905.05321 [astro-ph.HE].
- [26] A. Tursunov, Z. Stuchlík, M. Kološ, N. Dadhich, and B. Ahmedov, *Astrophys. J.* **895**, 14 (2020), arXiv:2004.07907 [astro-ph.HE].
- [27] K. Parfrey, A. Philippov, and B. Cerutti, *Phys. Rev. Lett.* **122**, 035101 (2019), arXiv:1810.03613 [astro-ph.HE].
- [28] T. Assumpção, V. Cardoso, A. Ishibashi, M. Richartz, and M. Zilhão, *Phys. Rev. D* **98**, 064036 (2018).

---

## BIBLIOGRAPHY

- [29] J. Shipley and S. R. Dolan, *Class. Quant. Grav.* **33**, 175001 (2016), arXiv:1603.04469 [gr-qc].
- [30] J. O. Shipley, *Strong-field gravitational lensing by black holes*, Ph.D. thesis, Sheffield U. (2019), arXiv:1909.04691 [gr-qc].
- [31] A. Bohn, W. Throwe, F. Hébert, K. Henriksson, D. Bunandar, M. A. Scheel, and N. W. Taylor, *Class. Quant. Grav.* **32**, 065002 (2015), arXiv:1410.7775 [gr-qc].
- [32] D. Christodoulou and R. Ruffini, *Phys. Rev. D* **4**, 3552 (1971).
- [33] I. Cabrera-Munguia, *Physics Letters B* **786**, 466 (2018).
- [34] V. Manko and E. Ruiz, *Physics Letters B* **794**, 36 (2019).
- [35] C. J. Ramírez-Valdez, H. García-Compeán, and V. S. Manko, *Phys. Rev. D* **102**, 024084 (2020).
- [36] L. T. Sanches and M. Richartz, *Phys. Rev. D* **104**, 124025 (2021).
- [37] S. Carroll, *Spacetime and Geometry: An Introduction to General Relativity* (Addison Wesley, 2004).
- [38] O. Semerák and M. Basovník, *Phys. Rev. D* **94**, 044006 (2016).
- [39] J. Ryzner and M. Žofka, *Class. Quant. Grav.* **32**, 205010 (2015), arXiv:1510.02314 [gr-qc].
- [40] G. Denardo and R. Ruffini, *Physics Letters B* **45**, 259 (1973).
- [41] D. Christodoulou, *Phys. Rev. Lett.* **25**, 1596 (1970).
- [42] E. Berti, R. Brito, and V. Cardoso, *Phys. Rev. Lett.* **114**, 251103 (2015).
- [43] Z. Stuchlík, *Bulletin of the Astronomical Institutes of Czechoslovakia* **31**, 129 (1980).
- [44] M. Patil, T. Harada, K.-i. Nakao, P. S. Joshi, and M. Kimura, *Physical Review D* **93**, 104015 (2016).

## BIBLIOGRAPHY

---

- [45] S. Mukherjee and R. K. Nayak, *Astrophysics and Space Science* **363**, 163 (2018).
- [46] A. Prasanna and N. Dadhich, *Il Nuovo Cimento B (1971-1996)* **72**, 42 (1982).
- [47] F. de Felice, F. Sorge, and S. Zilio, *Classical and Quantum Gravity* **21**, 961 (2004).
- [48] M. Bhat, S. Dhurandhar, and N. Dadhich, *Journal of Astrophysics and Astronomy* **6**, 85 (1985).
- [49] S. Parthasarathy, S. Wagh, S. Dhurandhar, and N. Dadhich, *The Astrophysical Journal* **307**, 38 (1986).
- [50] F. L. Dubeibe and J. D. Sanabria-Gómez, *Phys. Rev. D* **94**, (2016).
- [51] T. Baumgarte, *Numerical relativity : solving Einstein's equations on the computer* (Cambridge University Press, Cambridge, UK New York, 2010).
- [52] A. Bohn, W. Throwe, F. Hébert, K. Henriksson, D. Bunandar, M. A. Scheel, and N. W. Taylor, *Class. Quant. Grav.* **32**, 065002 (2015), arXiv:1410.7775 [gr-qc].
- [53] F. H. Vincent, E. Gourgoulhon, and J. Novak, *Classical and Quantum Gravity* **29**, 245005 (2012).